Nanoscale

ROYAL SOCIETY OF CHEMISTRY

MINIREVIEW

View Article Online
View Journal | View Issue

Cite this: *Nanoscale*, 2023, **15**, 5598

Recent developments in lead-free bismuth-based halide perovskite nanomaterials for heterogeneous photocatalysis under visible light

Zehong Wu,[a,b,c] Harun Tüysüz,[d] Flemming Besenbacher,[e] Yitao Dai *[a,b,c] and Yujie Xiong *[a,b]

Received 8th January 2023,
Accepted 16th February 2023

DOI: 10.1039/d3nr00124e

rsc.li/nanoscale

Halide perovskite materials, especially lead-based perovskites, have been widely used for optoelectronic and catalytic applications. However, the high toxicity of the lead element is a major concern that directs the research work toward lead-free halide perovskites, which could utilize bismuth as a promising candidate. Until now, the replacement of lead by bismuth in perovskites has been well studied by designing bismuth-based halide perovskite (BHP) nanomaterials with versatile physical–chemical properties, which are emerging in various application fields, especially heterogeneous photocatalysis. In this mini-review, we present a brief overview of recent progress in BHP nanomaterials for photocatalysis under visible light. The synthesis and physical–chemical properties of BHP nanomaterials have been comprehensively summarized, including zero-dimensional, two-dimensional nanostructures and hetero-architectures. Later, we introduce the photocatalytic applications of these novel BHP nanomaterials with visible-light response, improved charge separation/transport and unique catalytic sites. Due to advanced nano-morphologies, a well-designed electronic structure and an engineered surface chemical micro-environment, BHP nanomaterials demonstrate enhanced photocatalytic performance for hydrogen generation, CO_2 reduction, organic synthesis and pollutant removal. Finally, the challenges and future research directions of BHP nanomaterials for photocatalysis are discussed.

1. Introduction

Since Fujishima first reported TiO_2 photocatalysis for water splitting in 1972,[1] heterogeneous photocatalysis driven by semiconductor-based photocatalysts has attracted more and more attention due to its direct use of sustainable solar energy and mild reaction conditions.[2] In recent years, heterogeneous photocatalysis has been employed in various applications, such as photocatalytic H_2 generation,[3,4] CO_2 reduction,[5,6] decontamination of heavy metals and organic pollutants,[7,8] and organic synthesis.[9–12] In heterogeneous photocatalysis, the physical–chemical properties of photocatalytic materials, including elemental compositions, geometric/electronic structures and surface chemical environment, play key roles in promoting photocatalytic performance.[13–17] However, conventional photocatalysts such as TiO_2 and ZnO can only absorb ultraviolet light (accounting for only 5% of sunlight), which has severely limited the widespread usage of heterogeneous photocatalysis. In contrast, metal halide perovskites (MHPs) can exhibit desired visible or even near-infrared light absorption with narrow bandgaps, which can be facilely regulated by their versatile element compositions (different metal and halide species).[18–23] Moreover, the low-cost and facile synthesis of nanostructured MHPs with excellent electronic properties, such as long diffusion lengths of charge carriers (up to micrometers) and ultralow bulk defect density ($\sim 10^{10}$ cm^{-3} for single crystals), renders them intriguing for employment in the optoelectronic fields.[24–29] These advantages offer MHPs as promising photocatalytic materials with better light-harvesting capabilities, improved charge separation/transport and suitable catalytic sites on surface, which may lead to more efficient energy conversion from solar to chemical energy.[30] MHPs were first discovered in 1893,[31] but their research was not revived until Kojima *et al.* applied halide perovskites to solar cells in 2009.[32] Subsequently, lead-based halide perovskites have prevailed in the fabrication of semiconductor-based optoelectronic devices[33] and photocatalytic systems[34] mainly due to high bandgap tunability, outstanding charge mobility

---

[a] *Hefei National Laboratory for Physical Sciences at the Microscale, School of Chemistry and Materials Science, University of Science and Technology of China, Hefei, Anhui 230026, China. E-mail: yitaodai@ustc.edu.cn, yjxiong@ustc.edu.cn*
[b] *Key Laboratory of Precision and Intelligent Chemistry, University of Science and Technology of China, Hefei, Anhui 230026, China*
[c] *Suzhou Institute for Advanced Research, University of Science and Technology of China, Suzhou, Jiangsu 215123, China*
[d] *Max-Planck-Institut für Kohlenforschung, Mülheim an der Ruhr 45470, Germany*
[e] *Interdisciplinary Nanoscience Center (iNANO), Aarhus University, DK-8000 Aarhus C, Denmark*

and suitable redox capabilities. Unfortunately, the high toxicity and bioavailability of Pb as a heavy metal severely hinder the commercial applications of lead-containing perovskites due to the high risk of polluting the environment and damaging human health.[35,36]

In order to address the concerns about the environmental impact of MHPs, researchers are trying to replace the heavy metal (Pb) in halide perovskites with other more inert candidates such as Sn and Bi metals, *etc*.[37–43] However, the addition of Sn^{2+} always demonstrates undesired instability because of susceptibility to oxidation.[44] As the isoelectric ion of Pb^{2+}, Bi^{3+} is expected to be a suitable candidate to replace Pb^{2+}; this has been reported in several successful cases such as bismuth-based halide perovskites with high stability.[45–47] For example, $Cs_3Bi_2X_9$ (X = Cl, Br and I) nanocrystals have been prepared, *via* a simple antisolvent method, which exhibited blue emission with a photoluminescence efficiency of 0.2% and quite high stability towards air exposure for over 30 days.[48] Moreover, higher Lewis acidity of Bi^{3+} over Pb^{2+} gives the surface of BHP stronger acidic sites, thus enhancing the photocatalytic efficiency of BHP for acid-catalyzed organic reactions such as the ring-opening reaction of epoxides.[49] For several important photocatalytic reactions (*e.g.*, H_2 evolution,[50] CO_2 reduction[51] and H_2O_2 synthesis[52]), dozens of photocatalysts such as g-C_3N_4,[53] $ZnIn_2S_4$,[54] and Bi_2WO_6[55] have been well explored with satisfactory performance. In contrast, BHP photocatalysts, which possess more tunable bandgaps (varying from 1.8 to 3.1 eV) and diverse elemental compositions (*e.g.*, different halides and Ag/Cu atoms), need further research to investigate their photocatalytic applications in various reactions.

So far, there exist several reviews on the development of MHP-based photocatalysts including their composites in combination with other semiconductors.[34,56–62] Most of them discuss the synthesis, optical properties and photocatalytic applications of lead-containing MHPs. Some other reviews involving lead-free MHPs have mainly focused on their photoelectric properties and application in optoelectronic devices (*e.g.*, solar cells, light-emitting diodes, and photodetectors) and photocatalysis.[42,43,63–71] However, a dedicated review on the comprehensive analysis of BHP-based photocatalysts is still unavailable. Accordingly, this minireview summarizes the synthesis methods and physical–chemical properties of BHPs, with a focus on the fabrication of BHP nanomaterials with various micro-morphologies, band structures and surface chemical environment. Furthermore, we discuss recent applications of BHPs in heterogeneous photocatalysis, such as photocatalytic H_2 generation, CO_2 reduction, organic transformations, and degradation of organic dyes. Finally, an outlook on the rational design and synthesis of novel BHPs with more diverse nanostructures, satisfactory quantum yields, and stability is presented.

2. Photocatalytic principles and fundamental structures, compositions of BHPs

In photocatalytic reactions, the main roles of semiconductor-based photocatalysts involve light absorption with the generation of photoinduced electron–hole pairs and the transport of charge carriers to the surface for driving target redox reactions. The catalytic reaction processes usually require the existence of active sites on the surface to activate reactants after capturing charges. In detail, the fundamental steps occur as follows in the whole photocatalytic process (Fig. 1a):[11] (1) the semiconductor-based photocatalyst is excited by light, and

---

Zehong Wu

*Zehong Wu received his B.S. degree in polymer chemistry in 2019 from the University of Science and Technology of China (USTC). He is now a Ph.D. candidate at the USTC. His current research interest focuses on heterogeneous photocatalysis for organic synthesis by designing efficient photocatalytic nanomaterials (*e.g.*, lead-free halide perovskites).*

Harun Tüysüz

Harun Tüysüz gained his Ph.D. degree in chemistry in the Department of Heterogeneous Catalysis at the Max-Planck-Institut für Kohlenforschung (MPI-KOFO) in 2008 under the supervision of Prof. Ferdi Schüth and then conducted postdoctoral research with Prof. Peidong Yang at the University of California, Berkeley. In 2012 he was appointed as the head of the research group "Heterogeneous Catalysis and Sustainable Energy" at MPI-KOFO. His research group focuses on the design of nanomaterials for sustainable energy-related catalytic applications. His accomplishments have been awarded with several prizes including the Jochen Block Prize 2016, the DECHEMA Prize 2019, and the Forcheurs Jean-Marie Lehn Prize 2020.

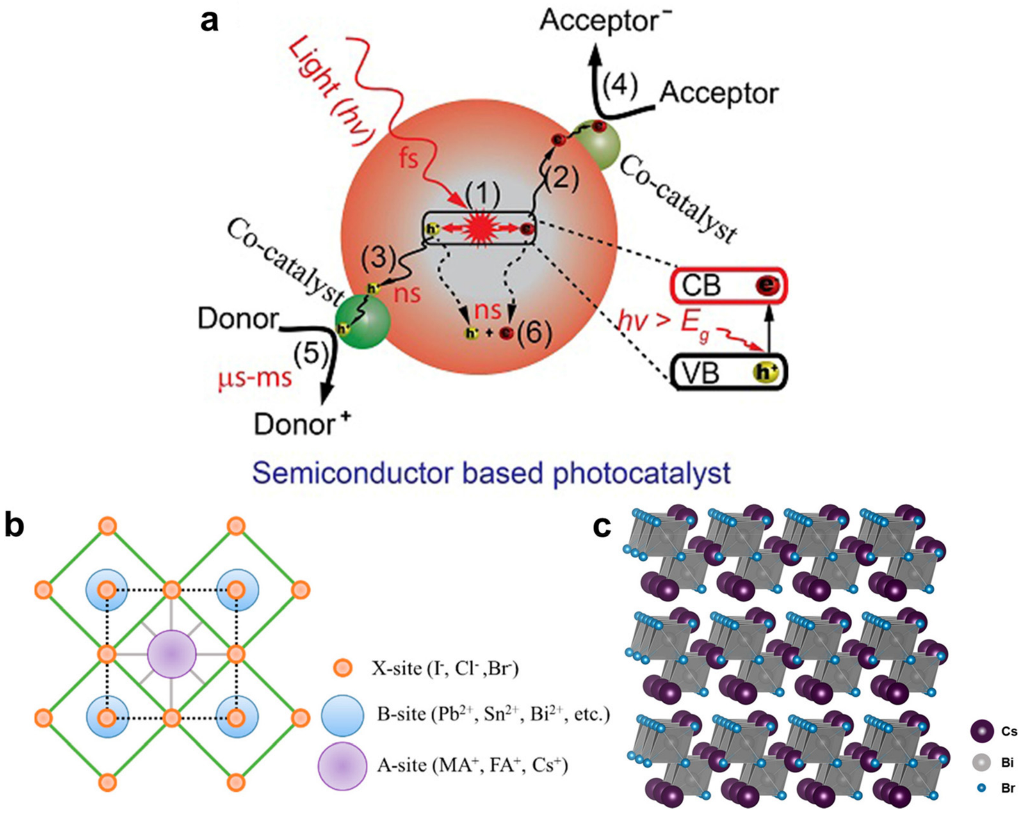

Fig. 1 (a) Fundamental working principles of a semiconductor-based photocatalyst. Reproduced with permission from ref. 11. Copyright 2022 Tsinghua University Press. (b) The typical crystal structure of MHPs. Reproduced with permission from ref. 73. Copyright 2020 MDPI. (c) The typical crystal structure of $Cs_3Bi_2Br_9$. Reproduced with permission from ref. 77. Copyright 2016 American Chemical Society.

photogenerated electrons jump to the conduction band (CB) from the valence band (VB), which accepts the left holes (step 1). This process happens quite rapidly at a femtosecond level ($\sim 10^{-15}$ s). (2) Subsequently, the electrons and holes are transferred to the photocatalyst's surface (steps 2 and 3). This charge diffusion occurs quickly as well, at a nanosecond scale ($\sim 10^{-9}$ s). (3) Finally, the electrons and holes approaching the surface are utilized by catalytically active sites (*e.g.*, co-catalysts) to initiate the desired redox reactions (steps 4 and 5), which is a quite slow process requiring microseconds to milli-

Flemming Besenbacher

Flemming Besenbacher received his Ph.D. from Aarhus University in Denmark in 1978. He is a professor and doctor of natural sciences at the Interdisciplinary Nanoscience Centre (iNANO) and the Department of Physics and Astronomy at Aarhus University. He is a member of the Danish Academy of Natural Sciences, the Danish Academy of Science and Technology, and the Royal Danish Academy of Sciences. He is engaged in the development and application of scanning probe microscopy and other surface science technologies, which have been applied in many fields such as physics, chemistry, biology, and medicine.

Yitao Dai

Yitao Dai received his B.S. in fine chemical engineering in 2011 and M.S. in applied chemistry in 2014 both from the Dalian University of Technology, later Ph.D. in nanoscience in 2018 from Aarhus University in Denmark. From 2018 to 2021, he worked as a post-doctoral researcher (Alexander von Humboldt Fellow) at Max-Planck-Institut für Kohlenforschung, Germany. He is currently a Research Professor at the University of Science and Technology of China (USTC). His research focuses on heterogeneous catalysis, including photocatalytic organic synthesis.

seconds (10^{-6}–10^{-3} s) in contrast to the above steps.[72] In addition, electron–hole pairs might recombine with each other, dissipating energy as fluorescence or heat in nanoseconds (step 6).

According to the above-mentioned photocatalytic principles, BHP could be an ideal photocatalyst due to its visible spectral tunability, long diffusion lifetime of carriers, and flexible surface chemical environment.[65] Generally, the crystal structure of a typical halide perovskite, ABX_3, consists of corner-shared $[BX_6]$ octahedra with A^+ ions occupying the cuboctahedra cavities (Fig. 1b).[73] A-site ion is usually a monovalent cation (*e.g.*, organic methylammonium (MA), formamidinium (FA), or inorganic Rb^+/Cs^+/Ag^+/Cu^+), while B-site ion typically corresponds to a divalent metal cation (such as Pb^{2+}, Ge^{2+} or Sn^{2+}).[69] The X-site ion indicates a halide anion (*e.g.*, Cl^-, Br^-, or I^-), which always strongly affects the VB position of MHP.[74,75] In addition, the value of Goldschmidt tolerance factor t ($t = \frac{R_A + R_X}{\sqrt{2}(R_B + R_X)}$ with R as the ionic radius of related ions) should locate between 0.8 and 1.1 to form a stable MHP.[76] In comparison, the replacement of divalent ions by trivalent Bi^{3+} ions leads to the structural derivation with a typical formula of $A_3Bi_2X_9$ for BHP materials, where only two-thirds of the octahedral center positions are completely occupied by Bi^{3+} in a two-dimensional layered perovskite structure (Fig. 1c).[77] Furthermore, the introduction of another monovalent cation can produce a halide double perovskite with a general formula of $A_2M(I)BiX_6$ (*e.g.*, $Cs_2AgBiBr_6$ or $Cs_2CuBiBr_6$), which demonstrates a three-dimensional perovskite structure analogous to ABX_3.[78–81] Besides, all-inorganic BHPs (*e.g.*, $Cs_3Bi_2Br_9$) with inorganic A-site cations can exhibit improved thermal and chemical stability compared with their organic–inorganic hybrid counterparts (*e.g.*, $MA_3Bi_2Br_9$).[82,83]

Yujie Xiong

Yujie Xiong received his B.S. in chemical physics in 2000 and Ph.D. in inorganic chemistry in 2004, both from the University of Science and Technology of China (USTC). During 2004–2009, he worked as a postdoc at the University of Washington in Seattle and as a Research Associate at the University of Illinois at Urbana-Champaign, respectively. He was Principal Scientist of the National Nanotechnology Infrastructure Network (NSF-NNIN) site at Washington University in St. Louis in 2009–2011. He joined USTC in 2011, and currently is the Chair Professor of Chemistry. His research centers on artificial cycles of elements and energy toward ecosystem reconstruction.

3. BHP photocatalysts: synthesis and properties

The physical–chemical properties of BHP nanomaterials are significant for their optoelectronic applications, including photocatalysis. These indispensable properties can be well regulated by the preparation protocols, which can precisely vary the micro-morphologies and elemental compositions of BHPs. In this section, the synthesis methods and properties of BHP nanomaterials in different dimensions will be introduced, including zero-dimensional (0D),[82,84–86] two-dimensional (2D) nanostructures[87,143] and hetero-architectures.[42,88,89] Notably, as far as we know, there are still few reports on 1D and 3D BHP nanomaterials, which can be regarded as promising research directions on material synthesis. Table 1 summarizes the typical BHP nanomaterials with versatile components (organic–inorganic hybrid perovskite or all-inorganic perovskite) based on synthesis approaches (including antisolvent recrystallization, hot-injection, solvothermal, rapid quenching, self-template-oriented method and other physical methods), nano-morphologies and optical properties. Additionally, it should be noted the dimension mentioned below relates to the morphological structure, not the crystal structure.

3.1 0D BHPs

0D materials refer to the microstructure size in a nanoscale range (1–100 nm) in three dimensions, mainly including very small quantum dots (QDs) and particles. 0D perovskite materials usually show superiority in optoelectronic properties that benefit from their particular size and structure. The typical 0D BHPs can be prepared by various approaches such as ultrasonication, ligand-assisted antisolvent precipitation, hot-injection, and ion-exchange process.[19,85,90,96] Ultrasonication from bulk crystals can provide a direct and simple method to obtain BHP nanocrystals. For example, S. Bhosale *et al.* applied an ultrasonic top-down method with the assistance of ligands to produce $Rb_3Bi_2I_9$, $Cs_3Bi_2I_9$, and $MA_3Bi_2I_9$ BHPs at a nanometer scale.[90] However, this ultrasonic process takes a long time (3–5 days) for preparation and fails to precisely modulate the nano-morphologies of BHPs. In contrast, antisolvent recrystallization, with a much shorter process time and better control of nanostructures, has attracted more attention for the synthesis of 0D BHP nanomaterials. Generally, in an antisolvent recrystallization process, the precursor (*e.g.*, bismuth bromide) is first dissolved in a suitable solvent (*e.g.*, DMSO), which is subsequently dropped into an anti-solvent to precipitate quantum dot crystals. In this process, some surfactants such as octylamine (OLA) and oleic acid (OA) are added as ligands to control the crystallization rate and stabilize the formed colloidal solution with a narrow particle-size distribution.

For instance, Tang and co-workers prepared a stable colloidal solution containing $MA_3Bi_2Br_9$ QDs by dissolving MABr and $BiBr_3$ in dimethylformamide (DMF) and ethyl acetate with *n*-octylamine to form the precursor solution, which was drop-

Table 1 Summery of the synthesis, morphology and property of BHP nanomaterials

Dimension	Elemental compositions	Synthesis methods	Morphology	Band gap	Emission property	Ref.
0D	$MA_3Bi_2Cl_9$	Anion exchange from $MA_3Bi_2Br_9$	QDs (3.05 nm diameter)	Not mentioned	PL peak = 360 nm; FWHM = 50 nm; PLQY = 15%	84
	$MA_3Bi_2Br_9$	Anti-solvent re-precipitation			PL peak = 423 nm; FWHM = 62 nm; PLQY = 12%	
	$MA_3Bi_2I_9$	Anion exchange from $MA_3Bi_2Br_9$			PL peak = 540 nm; FWHM = 91 nm; PLQY = 0.03%	
	$MA_3Bi_2I_9$	Ultrasonication from bulk crystal	7.6 nm NC	2.4 eV	PL peak = 558 nm; τ_{ave} = 0.64 ns	90
	$Cs_3Bi_2I_9$		6.2 nm NC	2.5 eV	PL peak = 578 nm; τ_{ave} = 0.89 ns	
	$Rb_3Bi_2I_9$		12.6 nm NC	2.4 eV	PL peak = 575 nm; τ_{ave} = 1.19 ns	
	Cs_3BiCl_6	Hot-injection method	Cubic NCs (9.8 ± 1.3 nm edge lengths)	Not mentioned	PL peak = 391 nm; FWHM = 60 nm	91
	Cs_3BiBr_6		cubic NCs (10.9 ± 1.5 nm edge lengths)			
	Cs_3BiBr_6	Anti-solvent re-precipitation	Branch-like NCs (1.6 nm diameter)	2.89 eV	PL peak = 438 nm; FWHM = 92.1 nm; PLQY = 22%	92
	$Cs_3Bi_2Br_9$	Anti-solvent re-precipitation	Quasi-spherical NCs (6 nm diameter)	Not mentioned	PL peak = 460 nm; FWHM = 45 nm; PLQE = 4.5%	48
	$Cs_3Bi_2I_9$	Hot-injection method	Polydisperse NCs (39.5 ± 9.3 nm diameter)	Absorbance maximum at 489 nm	Unclear	93
		Solvothermal	Hexagonal prisms NCs	2.10 eV	Not mentioned	94
	$Cs_2AgBiCl_6$	Anti-solvent re-precipitation	Quasi-sphere NCs (5.0 nm diameter)	Absorbance peak at 367 nm	PL peak = 395 nm; FWHM = 68 nm; PLQE = 6.7%	95
	$Cs_2AgBiBr_6$		Not mentioned	Absorbance peak at 440 nm	PL peak = 465 nm; FWHM = 82 nm; PLQE = 0.7%	
	Cs_2AgBiI_6		Not mentioned	Absorbance peak at 500 nm	PL peak = 575 nm; FWHM = 69 nm; PLQE < 0.1%	
	$Cs_2AgBiBr_6$	Hot-injection method	Cubic NCs (9.5 nm average size)	2.52 eV	PL peak = 625 nm; τ_{ave} = 7.5 ns	96
	$Rb_7Bi_3Cl_{16}$	Anti-solvent re-precipitation	Quasi-spherical NCs (1.85 ± 0.8 nm diameter)	3.27 eV	PL peak = 437 nm; FWHM = 93 nm; PLQY = 28.43%; τ_{ave} = 5.17 ns	97
	$Cs_2AgSb_{1-y}Bi_yX_6$ (X = Br, Cl; $0 \leq y \leq 1$)	Hot-injection method	Cube-shaped NCs (~10 nm diameter)	Absorption peak at ~430 nm	PL peak = 478 nm and 610 nm	98
2D	$(PEG6\text{-}NH_3^+)_nCs_{3-n}Bi_2Br_9$	Fast cooling	Nanosheets (360 ± 94 nm lateral width; 5.1 ± 1.1 nm thickness)	2.7 eV	Not mentioned	99
	$Cs_3Bi_2Cl_3I_6$	Hot-injection then quenching	Nanosheets (~5 μm lateral width; 2–4 nm thickness)	2.04 eV	PL peak = 496 nm; FWHM = 13 nm; τ_{ave} = 6.693 ns	100
	$Cs_3Bi_2Br_9$	Hot-injection then quenching	Parallelogram nanoplates (of 60–250 nm side length; 9 nm thickness)	Absorption peak at 380 nm	PL peak = 427 nm and ~455 nm; FWHM = 39 nm; PLQY = 0.54%	101
		Fast cooling in acid solution	Nanoplates (2–40 μm basal plane size; 100–500 nm thickness)	2.64 eV	PL peak = 480 nm	87
	$Cs_3Bi_2I_9$	Spin-coat and annealing	Hexagonal nanosheets (~15 μm lateral size; 57 nm thickness)	1.99 eV	PL peak = 642 nm; FWHM = 100 nm	102
		Hot-injection then quenching	Nanodiscs (30–55 nm lateral width; 2–6 nm thickness)	1.97 eV	PL peak = 580 nm	103
		Self-template-oriented method	Nanosheets (200 nm lateral size; 6–8 nm thickness)	1.90 eV	Not mentioned	104
	$Cs_2AgBiBr_6$	Hot-injection then quenching	Nanoplates (200 nm lateral size; 3–5 nm thickness)	2.01 eV	PL peak = 630 nm	105
	$Cs_2AgBiBr_6$	Solvothermal-quenching	Rectangular nanoplates (180 ± 130 nm edge length; 3.6–6 nm thickness)	2.06 eV	PL peak = ~640 nm	106

Table 1 *(Contd.)*

Dimension	Elemental compositions	Synthesis methods	Morphology	Band gap	Emission property	Ref.
Heterojunction	$MA_3Bi_2I_9/DMA_3BiI_6$	*In situ* growth	Rod-like DMA_3BiI_6 on sheet-like $MA_3Bi_2I_9$	1.99 eV	PL peak = ~650 nm	88
	$Cs_3Bi_2Br_9/Ti_3C_2T_x$	*In situ* growth	$Cs_3Bi_2Br_9$ NCs (6 nm average size) on monolayer $Ti_3C_2T_x$ nanosheets	2.47 eV	PL peak = ~500 nm; τ_{ave} = ~0.04 ns	107
	$Cs_3Bi_2I_9/Bi_2WO_6$	*in situ* growth	$Cs_3Bi_2I_9$ NCs (~7 nm average size) on Bi_2WO_6 nanosheets (50–100 nm size; 2.5 nm thickness)	$Cs_3Bi_2I_9$: 1.93 eV; Bi_2WO_6: 2.69 eV	Not mentioned	42
	$Cs_3Bi_2I_9/CeO_2$-3 : 1	Electrostatic assembly	$Cs_3Bi_2I_9$ nanosheets (200 nm lateral size; 6–8 nm thickness) on CeO_2 nanosheets (20–30 nm transverse size; 1.5 nm thickness)	$Cs_3Bi_2I_9$: 1.90 eV; CeO_2: 2.82 eV	Not mentioned	104
	$Cs_3Bi_2Br_9$/d-BiOBr	*In situ* growth	$Cs_3Bi_2Br_9$ nanodots (12.1 nm average size) on BiOBr nanosheets (4.5 nm thickness)	$Cs_3Bi_2Br_9$: 2.68 eV; d-BiOBr: 2.77eV	PL peak = 467 nm; τ_{ave} = 11.5 ns	108
	$Cs_3Bi_2Br_9/M\text{-}TiO_2$ $Cs_2AgBiBr_6/M\text{-}TiO_2$	*In situ* growth	$Cs_3Bi_2Br_9$ or $Cs_2AgBiBr_6$ nanodots (3.9–9.9 nm) on spherical mesoporous TiO_2 (15.8 nm pore size)	$Cs_3Bi_2Br_9$: 2.59 eV; $Cs_2AgBiBr_6$: 2.22 eV; M-TiO_2: 3.15 eV	PL peak = ~470 nm; τ_{ave} = 11.2 ns PL peak = ~640 nm; τ_{ave} = 11.3 ns	109
	$Cs_3Bi_2I_9/g\text{-}C_3N_4$	Ultrasonic mixing	$Cs_3Bi_2I_9$ particles (45–50 nm) anchoring to the g-C_3N_4 sheets	$Cs_3Bi_2I_9$: 1.88 eV; g-C_3N_4: 2.68 eV	Not mentioned	110
	$Cs_3Bi_2Cl_9$ QD /$(BiO)_2CO_3$	Ultrasonic mixing	$Cs_3Bi_2Cl_9$ nanoparticles (2.59 ± 0.6 nm particle size) on rose-like $(BiO)_2CO_3$	$Cs_3Bi_2Cl_9$: 3.05 eV; $(BiO)_2CO_3$: 3.35 eV	Not mentioned	111
	$Cs_3Bi_2Br_9$ QDs/ In_4SnS_8	*In situ* growth	$Cs_3Bi_2Br_9$ QDs (5.6 nm diameter) on In_4SnS_8 nanoflower (2–4 nm layer thickness)	$Cs_3Bi_2Br_9$: 2.94 eV; In_4SnS_8: 2.36 eV	PL peak = ~500 nm; τ_{ave} = 4.87 ns	112
	$Cs_3Bi_2Br_9$/CdS	*In situ* growth	$Cs_3Bi_2Br_9$ particles on CdS nanorods	$Cs_3Bi_2Br_9$: 2.65 eV; CdS: 2.44eV	Not mentioned	113
	$Cs_2AgBiBr_6/Ti_3C_2T_x$	Ultrasonic mixing	$Cs_2AgBiBr_6$ NCs (32.2 nm average size) on $Ti_3C_2T_x$ nanosheets	Absorption peak at ~435 nm	PL peak = ~660 nm	114
	$Cs_2AgBiBr_6@g\text{-}C_3N_4$	*In situ* growth	g-C_3N_4 shells (2–3 nm thickness) on $Cs_2AgBiBr_6$ particles	Absorption edge around 650 nm	PL peak = 645 nm	89
	$Cs_2AgBiBr_6$ /Sr_2FeNbO_6	Electrostatic assembly	$Cs_2AgBiBr_6$ NPs (20–50 nm particle size) on polyhedral-like Sr_2FeNbO_6 NPs (200–500 nm particle size)	$Cs_2AgBiBr_6$: 2.17 eV; Sr_2FeNbO_6: 2.04 eV	PL peak = ~610 nm; τ_{ave} = 3.14 ns	115
	$Cs_2AgBiBr_6/Bi_2WO_6$	*In situ* growth	Cubic $Cs_2AgBiBr_6$ NCs (average size: 10 nm) on Bi_2WO_6 nanosheets (40–100 nm lateral size; 3 nm thickness)	$Cs_2AgBiBr_6$: 2.04 eV; Bi_2WO_6: 2.48 eV	PL peak = ~575 nm; τ_{ave} = 5.39 ns	116

Notes: NC short for nanocrystal; NP short for nanoparticle; PL short for photoluminescence; FWHM short for full width at the half maximum; PLQY short for photoluminescence quantum yield; τ_{ave} means average lifetime.

wise added to the antisolvent octane with oleic acid under vigorous stirring.[84] After centrifuging at 8000 rpm for 10 min, a clear pale-yellow colloidal solution was obtained with stably dispersed $MA_3Bi_2Br_9$ QDs, whose average size in diameter was as small as 3.05 nm (Fig. 2a and b). Besides, high-resolution transmission electron microscopy (HRTEM) and X-ray diffraction (XRD) results revealed the trigonal crystal structure of this 0D BHP nanomaterial (Fig. 2d and e). Moreover, the photoluminescence quantum yield (PLQY) of $MA_3Bi_2Br_9$ QDs could reach 12% with the emission peak located at 423 nm (Fig. 2f). Based on the time-resolved PL decay profile, $MA_3Bi_2Br_9$ QDs exhibited excitation radiative recombination as the dominant path for fluorescent decay with a short-lived PL lifetime of 1.96 ns (Fig. 2g). Meanwhile, the PL emission peaks of $MA_3Bi_2X_9$ QDs can be easily tuned from 360 to 540 nm *via* varying the halide ions from Cl to I. Analogous to hybrid organic–inorganic BHPs, all-inorganic counterparts can be facilely prepared by this antisolvent method as well.[48] Without the usage of ligands, the formed $Cs_3Bi_2X_9$ (X = Cl, Br and I) nanocrystals demonstrated a quasi-spherical shape with an average size of 6 nm. The photoluminescent emission of $Cs_3Bi_2X_9$ nanocrystals was tuned from 400 to 560 nm by the facile change of halide anions, which was unfortunately accompanied by a quite low PLQY of 0.2%. Impressively, Lou *et al.* reported a dramatic improvement of PLQY up to 22% after covering the surface of $Cs_3Bi_2Br_9$ QDs with octylammonium bromide and oleic acid, which also rendered the Cl counterpart a high PLQY of 62%.[85] This promotion in optical properties was mainly attributed to the passivation of surface trap-states through steady ligand binding. In addition, the ligands on the surface can serve as a protective shell to enhance thermal stability with unchanged PLQY after heating $Cs_3Bi_2Br_9$ QDs at 180 °C for 1 h. Basically, the elemental variation of halide anions in BHP QDs efficiently tunes the range of light absorp-

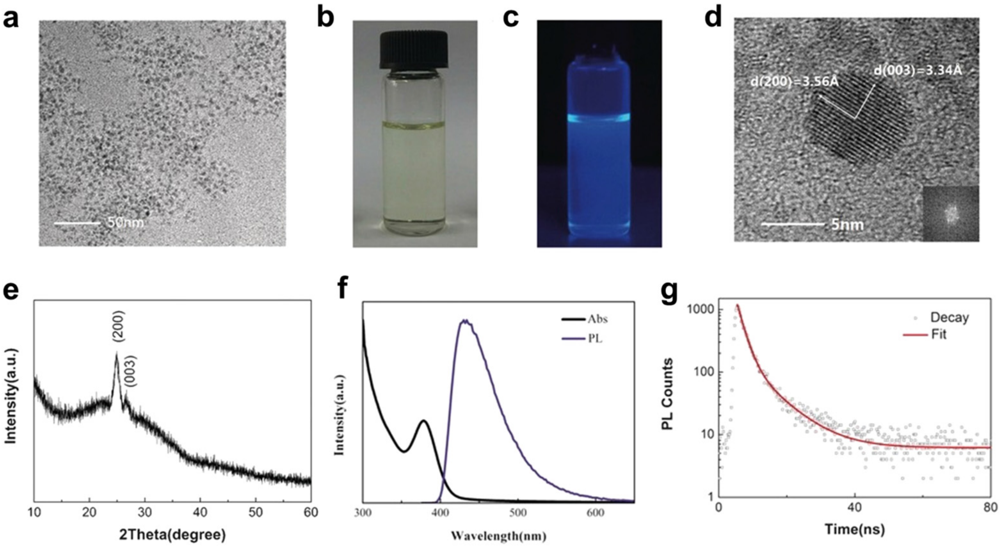

Fig. 2 Properties of $MA_3Bi_2Br_9$ QDs. (a) TEM image. (b) Typical optical image of a colloidal $MA_3Bi_2Br_9$ solution. (c) Colloidal $MA_3Bi_2Br_9$ solution under 365 nm UV light. (d) HRTEM image of a typical QD. The inset in the bottom right corner is the corresponding fast Fourier transform (FFT) image. (e) XRD patterns. (f) Absorption and PL spectra. (g) Time-resolved PL decay and fitting curve of a typical QD sample. Reproduced with permission from ref. 84. Copyright 2016 Wiley-VCH.

tion bands, while the surface chemical environment (*e.g.*, with or without ligands) significantly affects the intensity of photoluminescence.[82]

Moreover, the $Cs_3Bi_2X_9$ QD nanomaterials obtained by the antisolvent method can demonstrate halogen-associated catalytically active sites, successfully reducing CO_2 to CO under visible light.[86] In contrast to their Cl counterpart, the QDs with Br anions presented a narrower bandgap (2.62 eV), promoted charge separation/transport, and lower activation energy (1.84 eV) for the formation of $COOH^-$ intermediate. These superior physical–chemical properties of $Cs_3Bi_2Br_9$ QDs boosted the photocatalytic performance with a CO yield of 134.76 μmol g^{-1} and selectivity of 98.7%. In addition, another useful hot-injection method assisted with metal ion insertion led to the fabrication of $Cs_3Bi_2X_9$ (X = Cl or Br) nanocrystals with an average size of 11.8–13.3 nm, which involved the fast transformation (~5 min) from Cs_2BiX_6 nanocrystals in the presence of additional BiX_3 salts.[91] Furthermore, Zhou *et al.* reported the synthesis of $Cs_2AgBiBr_6$ cubic nanocrystals (the size of 9.5 nm) for the first time using a similar hot-injection method, where the Cs-oleate solution was injected into the 1-octadecene solvent containing $BiBr_3$, $AgNO_3$ and ligands (*e.g.*, OLA and OA) at 200 °C.[96] The as-prepared $Cs_2AgBiBr_6$ nanocrystals exhibited visible light absorption with a bandgap of 2.52 eV, indicating a blue shift in comparison with the bulk phase (1.95 eV) because of the quantum confinement effect in nanocrystals.[48] Meanwhile, the novel colloidal nanocrystals of Cs_2AgBiI_6, which are difficult to synthesize by direct methods, were successfully prepared *via* a post-ion-exchange approach.[117] Briefly, the exchange reaction between $Cs_2AgBiBr_6$ nanocrystals and trimethylsilyl iodide (TMSI) at room temperature in toluene for minutes produced the pure Cs_2AgBiI_6 phase. Different amounts of added TMSI reagent resulted in the generation of alloyed $Cs_2AgBiBr_{6-y}I_y$ ($0 \leq y \leq 6$), not the physical mixtures of Br and I counterparts. More I^- species gradually reduced the bandgap from 2.33 eV for $Cs_2AgBiBr_6$ to 1.75 eV for pure iodide, demonstrating the red shift of optical absorption edge from 500 to ~700 nm. TEM data clearly showed the slight change in particle size from 9.1 nm of $Cs_2AgBiBr_6$ to 9.9 nm of Cs_2AgBiI_6 nanocrystals. The analogous Cl to Br exchange occurred in the presence of $Cs_2AgBiCl_6$ nanocrystals and trimethylsilyl bromide. Notably, the anion redistribution could take place even between different nanocrystals, where the mixed solution of $Cs_2AgBiCl_6$ and $Cs_2AgBiBr_6$ led to the formation of an alloyed composition $Cs_2AgBiCl_{6-y}Br_y$ after several hours. However, these formed nanocrystals crashed out of the solution after exposure to light and air for a few days, which may be connected with the decomposition in the presence of water. On the whole, this anion-exchange method not only developed novel BHP materials with mixed halides that may be hard to prepare by direct-synthesis methods (*e.g.*, iodide ones), but also preserved the nanostructures of BHP precursors.[118] In addition to the anion-exchange, by adding other cations (Mn^{2+},Yb^{3+},*etc.*) into precursors, Mn/Yb-doped BHPs could be synthesized, which exhibited superior stability.[119,120]

So far, 0D BHP nanomaterials have been successfully synthesized by various methods. Compared with the complicated hot-injection and solvothermal method, antisolvent recrystallization can present a few advantages, such as mild synthesis conditions, large-scale preparation, and broad scope for different precursors. Furthermore, the electronic structure and physicochemical properties of 0D BHP nanomaterials can be precisely regulated by tuning the metal ions and halide species. However, the stability of 0D BHP nanomaterials with small sizes in aqueous phase or polar solvents still requires substantial improvement for practical applications.

3.2 2D BHPs

The reported cases have demonstrated that 2D perovskite nanosheets have better stability,[87,121] abundant active sites,[122] and shorter charge transfer distance from the bulk to the surface of photocatalysts.[123,124] The tunable thickness and preferential exposure of active crystal facets could bring 2D BHP nanomaterials improved stability and excellent photocatalytic activity. Compared with the bulk crystal materials with irregular shapes, the shorter charge transfer distance endows 2D BHP nanomaterials with faster charge transport and promotes charge separation. Generally, 2D BHP nanomaterials can be obtained by controlled crystallization and mechanical exfoliation processes. Through the regulation of synthesis parameters, the thickness of 2D BHP nanosheets can be precisely tuned from 2 to 500 nm. However, the synthesis of ultrathin BHP nanomaterials with atomic monolayers is still unavailable.

Recently, 2D BHP materials have been successfully synthesized by controlled crystal growth processes. For instance, Dai *et al.* provided a facile and rapid synthetic protocol to prepare $Cs_3Bi_2Br_9$ nanoplatelet crystals in one minute.[87] They used ethyl acetoacetate (EA) as the structure-directing agent, which selectively interacted with bismuth atoms *via* two carbonyl groups to control the crystal growth in an acidic solution. In detail, the halide precursors (CsBr and $BiBr_3$) and EA were first dissolved in a dilute H_2SO_4 solution. Then, the clear acidic solution was placed in liquid nitrogen for rapid cooling under vigorous stirring for ~1 min (Fig. 3a). The hexagonal 2D BHP nanoplatelets with a basal size of 2–10 μm and a thickness of ~100 nm could be fabricated. The size of the formed 2D materials varied from 100 to 500 nm by adjusting the concentrations of BHP precursors in diluted H_2SO_4 (Fig. 3b–f). The elemental mapping results from the nanoplatelet sample showed a quite homogeneous distribution of Cs, Bi, and Br elements in all regions (Fig. 3g–i). Furthermore, the quantitative analysis of elemental content based on energy dispersive X-ray spectroscopy (EDX) revealed that the ratio of Cs : Bi : Br corresponded to 3.2 : 2.0 : 8.9, matching well with the theoretical value (Fig. 3j). As shown in Fig. 3k, the intensity of photoluminescence peak (around 480 nm) correlates well with the thickness of $Cs_3Bi_2Br_9$ nanoplatelets. The larger and thicker microcrystals with fewer trap states exhibit weaker photoluminescence. Thus, the appropriate thickness affords $Cs_3Bi_2Br_9$ nanoplatelets the suppressed radiative recombination behavior of charge carriers and abundant active sites for the activation of C–H bonds. Due to the rigid framework of these platelet microcrystals with fewer defects and suppressed charge recombination, the $Cs_3Bi_2Br_9$ nanoplatelets demonstrated satisfactory photocatalytic performance of toluene oxidation to benzaldehyde with decent selectivity (≥88%) and stability (no deactivation after 36 h).

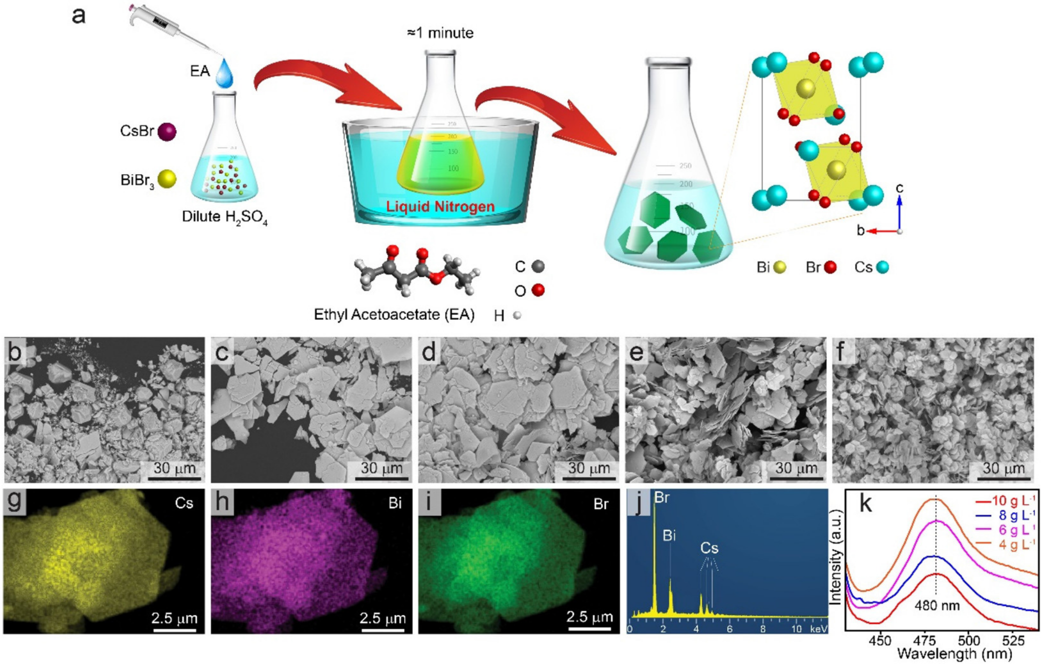

Fig. 3 (a) The synthesis procedure for $Cs_3Bi_2Br_9$ nanoplatelet microcrystals grown in dilute H_2SO_4 acidic solution with EA as directing agent *via* rapid cooling down in a liquid nitrogen bath for ~1 min. (b) Scanning electron microscope (SEM) image of the irregular crystals grown without the addition of EA. (c–f) SEM images of the platelet crystals grown in the presence of EA with different perovskite concentrations. (g–i) Scanning transmission electron microscopy (STEM)-based elemental mapping of the thinnest platelets. (j) SEM-EDX-based elemental analysis of the thinnest nanoplatelets. (k) Steady-state PL spectra of the $Cs_3Bi_2Br_9$ platelets synthesized with different perovskite concentrations (10, 8, 6, and 4 g L^{-1}). Reproduced with permission from ref. 87. Copyright 2021 Wiley-VCH.

Besides, given the important influence of temperature on the crystallization process, synthesis in a high-temperature environment (hot-injection or solvothermal method) followed by fast quenching in ice water becomes a distinctive method to fabricate 2D BHP nanosheets. For example, Kundu *et al.* reported the synthesis of 2D layered $Cs_3Bi_2I_6Cl_3$ by a hot-injection method followed by fast quenching.[100] They demonstrated that during the reaction temperature increase from 120 °C to 180 °C, the initially formed nanocrystals (Fig. 4a) transformed to nanosheets (with the lateral size of ∼5 μm and thickness of 2–4 nm) completely (Fig. 4b). In comparison with the bulk sample, the $Cs_3Bi_2I_6Cl_3$ nanosheets demonstrated a narrow and blue-shifted band-edge emission (peak at 520 nm) with a small Stokes shift (0.12 eV) (Fig. 4c–f). This may come from quantum confinement effect appearing on the unique 2D structure. Coincidentally, Huang *et al.* reported the effect of precursor concentrations on tuning the morphology of $Cs_2AgBiBr_6$.[105] By increasing precursor concentrations, they successfully controlled the morphology varying from 0D nanocubes to 2D nanosheets, which demonstrated the thickness of 3–5 nm and lateral size of ∼200 nm. The 2D $Cs_2AgBiBr_6$ nanosheets exhibited a strong absorption peak at ∼430 nm with the PL emission located at ∼630 nm. These results illustrated that high temperature and concentration may accelerate the diffusion of reactant and weaken the ligand–surface binding, which contribute to the fabrication of 2D nanosheets.

In addition, Ji *et al.* prepared $Cs_3Bi_2I_9$ hexagonal nanoplates by an ultrasound-based method, which exfoliated bulk BHP samples obtained from the antisolvent recrystallization process.[143] However, this physical exfoliation method failed to precisely control the thickness of the above $Cs_3Bi_2I_9$ nanoplates. Similarly, Qi *et al.* adopted the spin-coating and annealing approach to fabricate the film-like $Cs_3Bi_2I_9$ with a hexagonal shape (lateral size of ∼15 μm and thickness of 57 nm). The 2D BHP material can also be prepared by using a suitable structural template. For instance, Feng *et al.* synthesized 2D

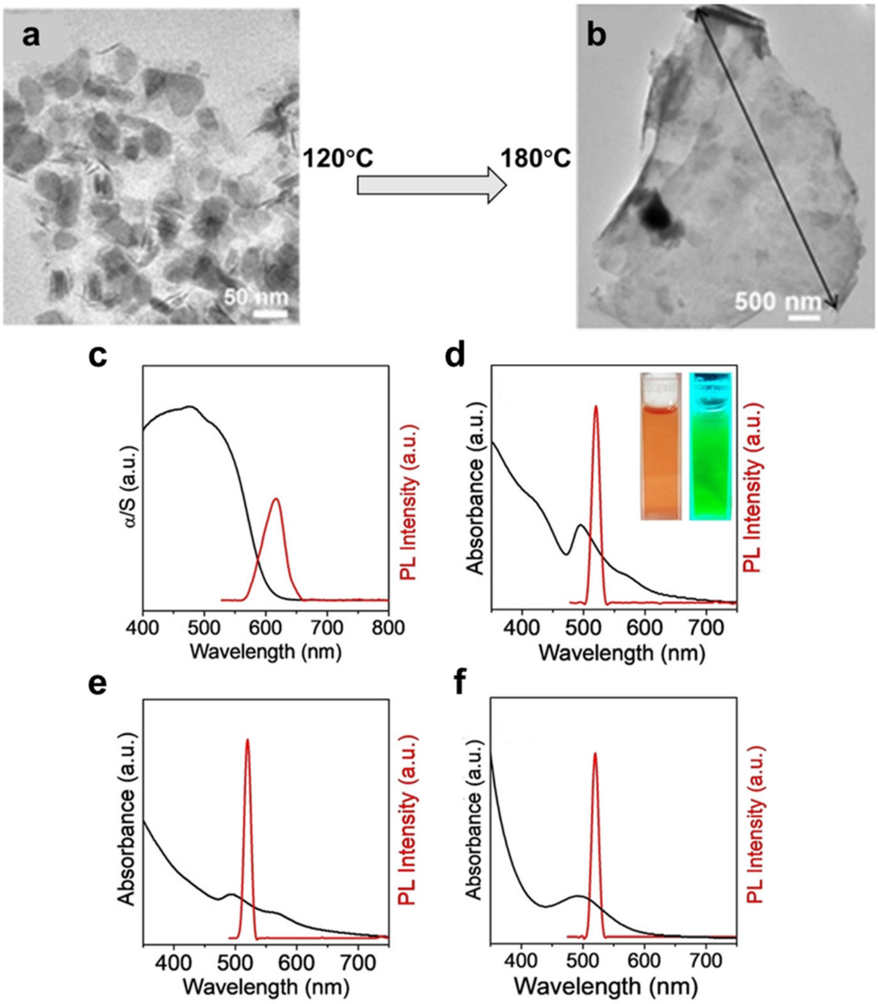

Fig. 4 (a) TEM image of $Cs_3Bi_2I_6Cl_3$ nanocrystals synthesized in 120 °C. (b) TEM image of $Cs_3Bi_2I_6Cl_3$ nanosheets synthesized in 180 °C. (c) Solid-state electronic absorption (α/S) (black) and PL (red) spectra of $Cs_3Bi_2I_6Cl_3$ bulk powders. (d–f) UV/Vis absorption (black) and PL (red) spectra of (d) $Cs_3Bi_2I_6Cl_3$ NCs, (e) $Cs_3Bi_2I_6Cl_3$ NCs-NSs, and (f) $Cs_3Bi_2I_6Cl_3$ NSs measured in solution phase. Inset in (d) is the photograph of NCs solution in the absence (left) and presence (right) of UV light. Reproduced with permission from ref. 100. Copyright 2021 Wiley-VCH.

lead-free halide perovskite ($Cs_3Bi_2I_9$) nanosheets by a self-templating method with $BiOI/Bi_2O_{2.7}$ nanosheets as the scaffold.[104] With the presence of HI and CsI in an alcohol solution, $BiOI/Bi_2O_{2.7}$ nanosheets with a thickness of 6 nm were gradually eroded by HI to release Bi^{3+} ions for the nucleation of $Cs_3Bi_2I_9$. Simultaneously, the nanostructure of $BiOI/Bi_2O_{2.7}$ was reprinted after its complete transformation to pure $Cs_3Bi_2I_9$ nanosheets with a thickness of around 6–8 nm. However, this self-template-oriented approach requires the complicated preparation of sacrificial materials and fails to control the lateral dimension of 2D nanosheets because of the vigorous corrosion process.

Overall, the synthesis of 2D BHP nanomaterials requires careful control of crystallization conditions with complicated processes (*e.g.*, high-temperature step plus rapid cooling). To precisely regulate the thickness and lateral size of 2D nanosheets, organic ligands or template materials are always essential to direct the growth orientation of BHP crystals. However, atomic ultra-thin 2D BHP nanomaterials are still unavailable. Besides, a more effective and simple synthesis method is needed to avoid the usage of ligands for the construction of a clean perovskite surface.

3.3 BHP heterostructures

To promote the charge separation with a longer lifetime and facilitate the redox reactions on the surface, the construction of heterojunction-based photocatalysts (such as type II, Z-scheme and Schottky junctions)[42,125–127] is considered as one promising protocol for improved photocatalytic efficiencies.[60] The main methods used to assemble BHP heterojunctions include *in situ* growth, electrostatic assembly and ultrasound mixing. Among them, the *in situ* growth method is the most common and effective method. For example, Tang *et al.* reported the synthesis of air-stable $MA_3Bi_2I_9/DMA_3BiI_6$ perovskite heterojunctions *via* a solvothermal *in situ* growth strategy.[88] During the solvothermal process, the added DMF co-solvent underwent hydrolysis to produce dimethylamine, which was easily protonated to form $[(CH_3)_2NH_2]^+$ ions (DMA^+) in the acidic environment. Thus, the rod-like DMA_3BiI_6 *in situ* grew on the surface of sheet-like $MA_3Bi_2I_9$, which was firstly formed due to the fast reaction between CH_3NH_2I and Bi^{3+} ions at room temperature before the solvothermal treatment. Besides, the state and composition of the final heterojunction product depended on the reactant concentration and reaction temperature. As expected, the optical absorption of this composite presented a combination of light responses from the respective pure phases. Correspondingly, the bandgap of the $MA_3Bi_2I_9/DMA_3BiI_6$ composite should lie between that of the pure phases, which does not agree with the conclusion in the paper that the heterojunction had the smallest bandgap of 1.99 eV. Furthermore, the as-prepared type II $MA_3Bi_2I_9/DMA_3BiI_6$ heterojunction accelerated the diffusion of charge carriers with improved charge mobilities, offering an extended diffusion lifetime of ~38 ns and a lower charge transfer resistance of 1.15 kΩ cm^2. Eventually, the $MA_3Bi_2I_9/DMA_3BiI_6$ heterojunction exhibited promoted photocatalytic H_2 evaluation (rate of 198.2 μmol h^{-1} g^{-1}) without any co-catalyst under visible light irradiation.

On the other hand, the formation of a direct Z-type heterojunction by 2D/2D contact can be another effective route to fabricate advanced photocatalysts with improved photocatalytic performance.[128] Firstly, the large interfacial contact areas, abundant charge transfer channels and shortened charge transfer distance of 2D/2D heterojunctions benefit the rapid transfer and separation of photogenerated charge carriers. Secondly, the Z-type heterojunction can maximally maintain the redox ability of each component.[128] As shown in Fig. 5a, Feng *et al.* constructed a Z-type heterojunction of $Cs_3Bi_2I_9/CeO_2$ by simple electrostatic assembly (Fig. 5a).[104] The $Cs_3Bi_2I_9$ and CeO_2 nanosheets were fully dispersed in n-hexane with ultrasonic mixing and continuous stirring. Due to the attraction of the surface electrostatic charges, these two components were successfully assembled into the heterojunctions. TEM and elemental mapping analysis clearly indicated the close contact between $Cs_3Bi_2I_9$ and CeO_2 nanosheets (Fig. 5b–h). Furthermore, X-ray photoelectron spectroscopy (XPS) tests under light irradiation clearly showed the positive shifts (0.1–0.29 eV) of the binding energies from Ce 3d and O 1s, while two new signals appeared at lower energy positions for Bi 4f (Fig. 5i–k). This suggests the efficient electron transfer behavior from CeO_2 to $Cs_3Bi_2I_9$ nanosheets due to the presence of Z-scheme heterojunctions. Moreover, based on the results from electron paramagnetic resonance (ESR) tests, most holes were transferred from $Cs_3Bi_2I_9$ to accumulate on the CeO_2 phase with the strengthened DMPO-$OH^{\bullet}$ signal by oxidation water (Fig. 5l). Therefore, the Z-scheme heterojunction of $Cs_3Bi_2I_9/CeO_2$ can provide powerful electronic modulation to separate charges with enhanced redox capabilities, consequently showing excellent activity for CO_2 photoreduction with a high electron consumption rate of 877 μmol g^{-1}.

On the whole, several preparation methods such as ultrasonic mixing, electrostatic assembly, and *in situ* growth have been applied to fabricate BHP heterojunctions.[42,104,110,114] Compared with pristine BHP materials, the combination of BHP with other semiconductors (such as TiO_2, C_3N_4, CdS, Sr_2FeNbO_6) can engineer band structures with Z-scheme or type-II heterojunctions. The charge diffusion path and electron–hole recombination are thus optimized in these composites, which can dramatically promote their photocatalytic performance.[89,109,113,115]

4. Applications of BHP photocatalysts

Compared with homogeneous photocatalysis, heterogeneous photocatalysis demonstrates the following merits:[129] (1) facile separation and recovery of solid-state photocatalysts. (2) Lower costs in the preparation of photocatalysts. Cheap inorganic compounds or organic precursors are adopted in the heterogeneous cases, while expensive metal complexes are usually required in homogeneous photocatalysis. (3) Potential for

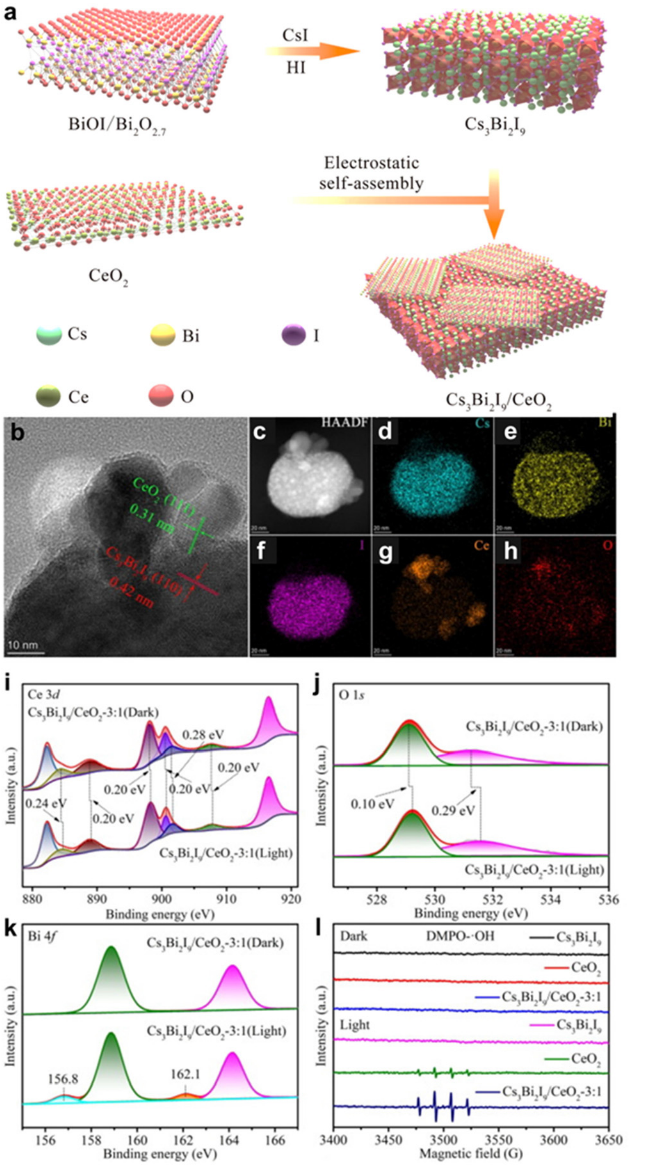

Fig. 5 (a) The preparation of $Cs_3Bi_2I_9$ nanosheets and the self-assembly between $Cs_3Bi_2I_9$ and CeO_2 nanosheets. (b) HRTEM image of $Cs_3Bi_2I_9/CeO_2$-3 : 1 assembly. (c–h) High-angle annular dark field (HAADF) image and elemental mapping images of $Cs_3Bi_2I_9/CeO_2$-3 : 1. (i–k) High-resolution XPS spectra of (i) Ce 3d, (j) O 1s and (k) Bi 4f for $Cs_3Bi_2I_9/CeO_2$-3 : 1 under dark and light excitation. (l) ESR spectra of $Cs_3Bi_2I_9$, CeO_2 and $Cs_3Bi_2I_9/CeO_2$-3 : 1 with DMPO as the radical trap. Reproduced with permission from ref. 104. Copyright 2021 Science Press and Dalian Institute of Chemical Physics, Chinese Academy of Sciences.

large-scale and continuous production modes *via* fixed-bed reactors.[130] Given the advantages of a high light absorption coefficient, tunable band structures, versatile surface chemical environment and good stability, BHP nanomaterials can serve as promising heterogeneous photocatalysts with visible-light response for various significant reactions. In recent years, several BHP nanomaterials have been applied for diverse photocatalytic reactions under visible light, including H_2 generation,[88,103,131] CO_2 reduction,[42,104,132] organic synthesis,[49,87,133] pollutant degradation[134] and photoinduced polymerization.[135,136]

4.1 H_2 generation

Photocatalytic H_2 generation has received great interest for the green production of hydrogen fuel and the storage of sustainable solar energy.[137,138] Recently, BHP photocatalysts have been explored for hydrogen production with decent activity under visible light illumination.[45] Since BHP materials are easily decomposed in water, most of the photocatalytic hydrogen generation tests using BHP materials were carried out in acidic HX (X = Br, I) solutions(a few in ethanol or aqueous solution). The presence of halide ions from HX acids can suppress the reaction equilibrium of BHP decomposition and enhance the stability of BHP materials. Table 2 summarizes photocatalytic H_2 production performance with different reaction conditions over BHP photocatalysts.

Guo *et al.* prepared an organo-inorganic hybrid perovskite material $(CH_3NH_3)_3Bi_2I_9$ by a simple hydrothermal method, which presented a photocatalytic hydrogen production rate of 12.19 μmol g^{-1} h^{-1} in HI solution.[45] After platinum was deposited as a co-catalyst, the rate for H_2 evolution approached 169.21 μmol g^{-1} h^{-1} due to the improved charge separation and more active sites. Obviously, the addition of platinum gives an outstanding improvement in photocatalytic H_2 generation rates.[45,110,139,140,142,145] However, the natural scarcity and high price of noble metals limit their wide application. Therefore, designing high-performance BHPs for photocatalytic H_2 generation without noble metals is challenging. Modulating the nanostructures of BHPs to improve photocatalytic H_2 evolution performance may be a promising approach. Ji *et al.* applied $Cs_3Bi_2X_9$ nanosheets to photocatalytic H_2 evolution in ethanol solutions.[143] The $Cs_3Bi_2I_9$ nanosheets with a coplanar octahedral structure afford the shortest Bi–Bi distance, which is beneficial for carrier transport, significantly enhancing the photocatalytic H_2 evolution rate (2157.8 μmol h^{-1} g^{-1}) (Fig. 6a). The photocurrent response of the photocatalysts (Fig. 6b) and recycling experiments illustrated that the $Cs_3Bi_2I_9$ nanosheets could maintain photocatalytic activity for several cycles with the satisfactory stability. In a similar way, Li *et al.* fabricated ordered BHPs $Cs_3Bi_2I_9$ hexagonal prisms with well-defined (100) and (006) facets (Fig. 6c).[94] Photogenerated holes and electrons in the nanocrystals were spatially separated to (100) and (006) facets, respectively, owing to a built-in electric field between the crystalline facets of ∼130 meV in these hexagonal prisms (Fig. 6d). Thus, $Cs_3Bi_2I_9$ hexagonal prisms showed outstanding activity for photocatalytic H_2 generation (1504.5 μmol h^{-1} g^{-1}) by HI splitting. Obviously, the well-designed nanostructure of $Cs_3Bi_2I_9$ crystals with the prism morphology could orientate the charge diffusion direction to improve the separation of electron–hole pairs, consequently resulting in the enhanced H_2 evolution. Although this $Cs_3Bi_2I_9$ photocatalyst showed stability over 8 h irradiation, some tiny solid iodine (I_2) particles were generated on the (100) facets (Fig. 6e), which may have a negative impact on the photocatalyst over a longer time

Table 2 Summary of recent photocatalytic H_2 generation over BHP nanomaterials

Catalyst	Solution	Irradiation conditions	Performance (μmol g^{-1} h^{-1})	Stability (h)	Ref.
$PtI_x/[(CH_3)_2NH_2]_3[BiI_6]$	$H_3PO_2/HI = 4:1$	425 nm LED Lamp	46.625	>100	139
$Pt/MA_3Bi_2I_9$	Aqueous HI solution	300 W Xe-lamp ($\lambda \geq 400$ nm)	169.21	>70	45
$Pt/MA_3Bi_2Cl_{8.8}I_{0.2}$	Saturated HCl/HI solution/H_3PO_2	300 W Xe-lamp ($\lambda \geq 420$ nm; 100 mW cm^{-2})	341 ± 61.7	5	140
$Pt\text{-}DA_3BiI_6$	HI and DAI solution	LED lamp	216	5	141
$Pt/Cs_3Bi_2I_9$ nanodiscs	Aqueous HI solution/H_3PO_2	AM 1.5G (150 mW cm^{-2})	225	8	103
$Pt/Cs_3Bi_{0.6}Sb_{1.4}I_9$	Aqueous HI solution	AM 1.5G (100 mW cm^{-2})	926	50	110
$Pt/Cs_3Bi_2I_9/g\text{-}C_3N_4$	MeOH aqueous solution	450 W Xe-lamp	920.76	6	110
$Pt/Cs_3Bi_2Br_9/g\text{-}C_3N_4$	Distilled water containing 10% triethanolamine	1500 W Xenon lamp (300–800 nm; 500 W m^{-2})	1050	6	142
$Cs_3Bi_2I_9$ nanosheets	Ethanol solution	300 W Xe lamp (790 mW cm^{-2})	2157.8	2	143
$Cs_3Bi_2I_9$ hexagonal prisms NCs	HI/ethyl acetate	AM1.5G (100 mW cm^{-2})	1504.5	8	94
$MA_3Bi_2I_9/DMA_3BiI_6$	Aqueous HI solution	300 W Xe-lamp ($\lambda \geq 420$ nm; 100 mW cm^{-2})	198.4	100	88
$Cs_2AgBiBr_6$/RGO	Saturated HBr and H_3PO_2 solution	300 W Xe-lamp ($\lambda \geq 420$ nm)	48.9	120	131
$Cs_2AgBiBr_6$/nitrogen-doped carbon (N–C)	Aqueous HBr solution	300 W Xe-lamp ($\lambda \geq 420$ nm; 100 mW cm^{-2})	380	24	144

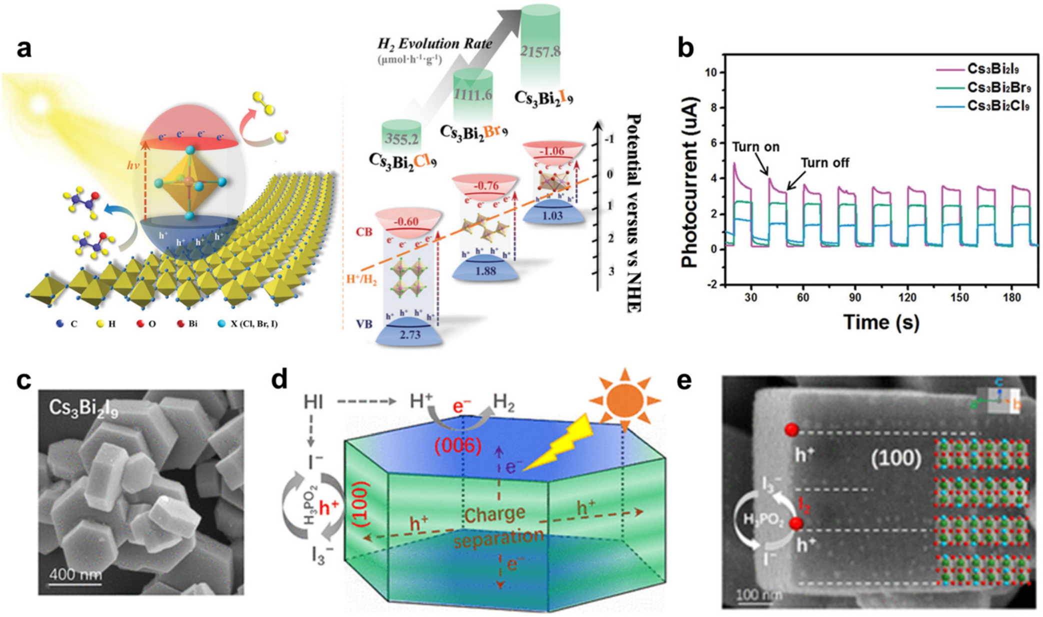

Fig. 6 (a) Schematic mechanism of H_2 evolution by $Cs_3Bi_2X_9$ nanosheets in ethanol. (b) Transient photocurrent responses of the photocatalysts. Reproduced with permission from ref. 143. Copyright 2022 Wiley-VCH. (c) Morphology and crystalline structure of $Cs_3Bi_2I_9$ hexagonal prisms. (d) H_2 production process and anisotropic charge transfer to the different redox facets. (e) SEM image of the photocatalysts after reaction for 8 h. Reproduced with permission from ref. 94. Copyright 2022 American Chemical Society.

test by covering active sites and blocking light absorption. These works demonstrated that it is possible to fabricate 0D or 2D high-efficiency BHP-based photocatalysts by regulation of geometric structures (constructing nanocrystals, or nanosheets, or prisms) and surface chemical micro-environment (decorating co-catalysts).

On the other hand, the photocatalytic performance of BHPs may be improved by combining them with other semiconductors to establish nanocomposites, which offer improved charge diffusion and diverse surface chemical environments.[60] For example, Wang *et al.* synthesized a composite consisting of $Cs_2AgBiBr_6$ (CABB) and reduced graphene oxide (RGO) for photocatalytic hydrogen production in a saturated HBr solution (Fig. 7a).[131] The CABB/RGO composite presented higher photocatalytic activity than pristine CABB due to the contribution from RGO with promoted charge separation/transport. Under visible light irradiation, the hydrogen production rate of the CABB/RGO photocatalyst reached up to 489 μmol g^{-1} within 10 h when the loading of RGO was 2.5% (Fig. 7b). Meanwhile, CABB/2.5% RGO remained stable after consecutive irradiation of 120 hours (Fig. 7c). Based on the mechanistic study, firstly CABB generated electrons and holes as the light

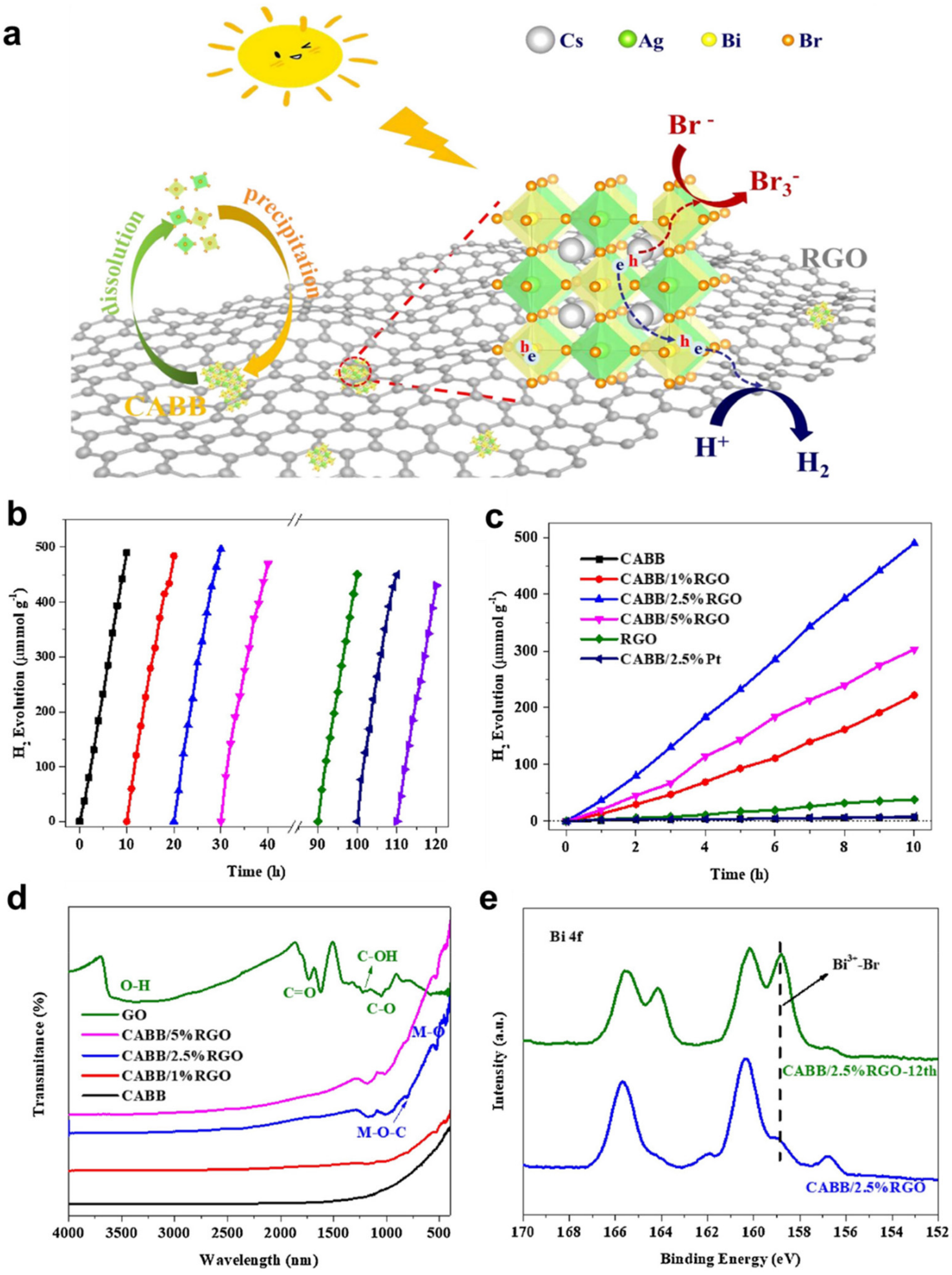

Fig. 7 (a) The photocatalytic H_2 generation over $Cs_2AgBiBr_6$/RGO (CABB/RGO) under visible light irradiation. (b) H_2 evolution activities of as-prepared catalysts, including CABB /*x*RGO composites with different contents of RGO, Pt/CABB, the pristine CABB and RGO. (c) The cycling tests of CABB/2.5%RGO for photocatalytic H_2 generation. (d) FTIR spectra of CABB/*x*RGO composites, CABB, and GO. (e) Bi 4f of CABB/2.5%RGO before and after 12 cycles of photocatalytic H_2 evolution tests. Reproduced with permission from ref. 131. Copyright 2019 Elsevier.

absorber under visible light irradiation. Then, the photogenerated electrons could transfer to conductive RGO through the M–O–C bonds, which was suggested by Fourier transform infrared (FTIR) spectra of as-prepared samples (Fig. 7d). Subsequently, the electrons reduced H^+ to H_2 at the active sites of RGO. Meanwhile, Br^- was oxidized to Br_3^- by the holes on the surface of CABB nanoparticles. Besides, the XPS measurement indicated that the chemical environment of bismuth species on the catalyst surface was changed after 12 cycles of photocatalytic H_2 evolution tests (Fig. 7e). These characterization data may suggest the recrystallization of CABB or the generation of other unclear bismuth species as active sites during photocatalysis. It should be noted that the nature of active sites on RGO for H_2 evolution is mysterious as well. These active sites play key roles since they not only capture the electrons from CABB but also provide the adsorption sites for hydrogen atoms. In addition to pure carbon materials, some nitrogen-containing carbon materials (C_3N_4 or N–C) have been combined with BHPs to promote photocatalytic H_2 evolution as well.[110,144]

Even though BHPs have exhibited photocatalytic activity in hydrogen evolution under visible light, the essential presence of the HX acidic environment limits their practical applications due to the corrosive nature and high cost of HX species. More research work should be performed to design robust BHP photocatalytic systems. For example, the core–shell nanomaterials with protective and active shells encapsulating BHP cores may drive the whole water splitting under neutral conditions.[14,146]

4.2 CO_2 reduction

Reducing atmospheric carbon dioxide levels is significant for environmental remediation to achieve ambitious climate goals such as net-zero greenhouse gas emissions by 2050.[147] Among diverse technologies for CO_2 reduction, solar-driven photocatalytic CO_2 reduction has gained much attention due to the clean and sustainable process of photocatalysis with the production of valued chemicals (*e.g.*, CH_4, CH_3OH, or HCOOH).[15] Table 3 summarizes recent studies about BHP photocatalysts for CO_2 reduction, including liquid-phase and gas–solid reaction systems. Recently, BHP materials have been employed as promising photocatalysts for CO_2 reduction. In the photocatalytic reduction of CO_2 to CO at the gas–solid interface with H_2O as a hydrogen source, a series of $A_3Bi_2X_9$ (A = Cs, Rb, MA; X = Br, I) nanocrystals was systematically investigated.[90,132] The photocatalytic activities of CO_2 reduction over various BHP photocatalysts under visible light irradiation demonstrated a trend of $Cs_3Bi_2I_9 > Rb_3Bi_2I_9 > MA_3Bi_2I_9 \gg TiO_2$.[90] The poor activity from TiO_2 mainly came from its wide bandgap without visible-light response. For the case of organic–inorganic BHP of $MA_3Bi_2I_9$, its self-oxidation of MA species by holes and the restricted charge transport retarded CO_2 photoreduction. In contrast, $Cs_3Bi_2I_9$ presented much higher activities with a methane yield of 14.9 μmol g^{-1} and CO yield of 77.6 μmol g^{-1}. In combination with the superior charge transfer in $Cs_3Bi_2I_9$, the BiI_6 units as Lewis acid sites could form complexes with CO_2 to offer the chemisorption of CO_2, synergistically resulting in the high photocatalytic activity for CO_2 reduction. Furthermore, the modification of halide species of $Cs_3Bi_2X_9$ (X = Br, I) could tune the activity and selectivity for CO_2 photoreduction. As a result, $Cs_3Bi_2(Br_{0.5}I_{0.5})_9$ NCs exhibited the optimal activity with 54 μmol g^{-1} of CO yield and 100% CO selectivity under visible light.[132] This selective photocatalytic performance mainly originated in the suitable band structure of $Cs_3Bi_2(Br_{0.5}I_{0.5})_9$ with a broad light absorption range, which led to the generation of abundant photoinduced charges with suitable redox capability.

Besides, double perovskite-based nanomaterials have also been applied in CO_2 photoreduction. In 2018, Zhou *et al.* reported that $Cs_2AgBiBr_6$ photocatalysts prepared by a hot-injection method converted CO_2 into CO and CH_4 under simulated sunlight with an electron consumption of 105 μmol g^{-1}.[96] After washing away the ligands on the surface, the photocatalytic performance was further promoted with a quantum efficiency of 0.028% at 398 nm due to the removal of ligand shells, which may dampen the transfer of charges from photocatalysts to reactants. However, the solvent of this photocatalytic system was an organic compound (*i.e.*, ethyl acetate), which may be the real source for the production of CH_4 or CO under light irradiation in the presence of perovskite photocatalysts.[90] Thus, the isotopic labeling test is required by use of $^{13}CO_2$ to evidence the occurrence of CO_2 photoreduction if there are other organic species in the system. Later, the Cs_2AgBiI_6 nanocrystals synthesized by the antisolvent recrystallization also exhibited highly selective CO_2 photoreduction with a CO yield of 18.9 μmol g^{-1} and 100% CO selectivity.[149] The usage of organic toluene as a solvent for CO_2 reduction may introduce carbonaceous contamination as well.

The fabrication of heterojunctions *via* combining BHPs with other semiconductors can further improve the catalytic

Table 3 Summary of recent photocatalytic CO_2 reduction over BHP materials

			Performance (μmol g^{-1} h^{-1})		
Catalyst	Reaction solution	Irradiation conditions	CO	CH_4	Ref.
$Cs_3Bi_2Br_9$ QDs	Gas–solid reaction system	AM 1.5G	26.95	—	86
$Cs_3Bi_2(Br_{0.5}I_{0.5})_9$ NCs	Gas–solid reaction system	300 W Xe lamp ($\lambda \geq 420$ nm)	18	—	132
$Cs_2NaBiCl_6$ porous microsphere	Gas–solid reaction system	300 W Xe lamp	30.22	1.12	148
$Cs_2AgBiBr_6$ NCs (washed)	Ethyl acetate	AM 1.5G (150 mW cm^{-2})	2.35	1.6	96
$Cs_2AgBiBr_6$ NPs	Ethyl acetate	a 405 nm laser diode	1	0.67	106
Cs_2AgBiI_6 NCs	Gas–solid reaction system	300 W Xe lamp ($\lambda \geq 420$ nm)	6.3	—	149
$Cs_3Bi_2I_9/Bi_2WO_6$	Gas–solid reaction system	Xe lamp (100 mW cm^{-2})	7.3	—	42
$Cs_2AgBiBr_6$@g-C_3N_4	Ethyl acetate/methanol	Xenon lamp (AM 1.5G; 150 mW cm^{-2})	0.6	1.5	89
$Cs_3Bi_2Br_9$/MCM-41	Gas–solid reaction system	300 W Xe lamp (350 mW cm^{-2})	17.24	—	150
$Cs_3Bi_2I_9/CeO_2$	Gas–solid reaction system	300 W Xe lamp (200 mW cm^{-2})	15	5	104
$Cs_2AgBiBr_6/Sr_2FeNbO_6$	Ethyl acetate/H_2O	300 W Xe lamp ($\lambda \geq 420$ nm)	50.00	8.12	115
$Cs_2AgBiBr_6$-Cu-RGO	Gas–solid reaction system	300 W Xe lamp (AM-1.5G)	1.9	10.7	151
$TiO_2/Cs_3Bi_2Br_9$ nanodots	Isopropanol	300 W Xe lamp (λ = 200–1100 nm; 70 mW cm^{-2})	4.54	24.2	109
$TiO_2/Cs_2AgBiBr_6$ nanodots			4.19	32.9	
$Cs_3Bi_2Br_9$ QDs/In_4SnS_8	Gas–solid reaction system	300 W argon lamp ($\lambda > 420$ nm)	9.55	—	112
$Cs_2AgBiBr_6/Ti_3C_2T_x$	Gas–solid reaction system	Xe lamp ($\lambda > 400$ nm; 150 mW cm^{-2})	11.1	1.3	114
$Cs_2AgBiBr_6/Bi_2WO_6$	Ethyl acetate/isopropanol	300 W Xe lamp (AM-1.5G; 100 mW cm^{-2})	42.19	0.41	116

activity of CO_2 photoreduction through promoted charge separation/transport. Liu *et al.* designed the *in situ* growth of $Cs_3Bi_2I_9$ crystals on the surface of $BiWO_6$ nanosheets to construct a Z-type heterojunction.[42] Because of the shared bismuth atoms at the interface between $BiWO_6$ and $Cs_3Bi_2I_9$, the formed strong interaction could promote the interfacial charge transfer (Fig. 8a). As a result, the CO_2-to-CO conversion rate of $Cs_3Bi_2I_9/Bi_2WO_6$ heterojunction incredibly grew up to 66 μmol g^{-1} (Fig. 8b), which was more than four times higher than that of pristine $Cs_3Bi_2I_9$ nanocrystals or their physical mixture ($Cs_3Bi_2I_9 \cdot Bi_2WO_6$). As shown in Fig. 8c, the $Cs_3Bi_2I_9/Bi_2WO_6$ photocatalyst could retain photocatalytic performance over three cycles. However, the increase in CO production rate was non-linear, which might be caused by the adsorption of some organic products on the surface of heterojunctions. Moreover, the photoinduced electrons from Bi_2WO_6 could effectively transfer to $Cs_3Bi_2I_9$ in the composite, which was evidenced by the negative shifts (0.2–0.35 eV) of binding energies from Cs 3d and I 3d and the positive shifts in W 4f and O 1s spectra based on *in situ* XPS measurements (Fig. 8d–g). This charge transportation matched well with the proposed Z-type heterojunction mechanism, bringing enhanced charge separation for superior photocatalytic properties. Similarly, Sun *et al.* reported halide perovskites CBB ($Cs_3Bi_2Br_9$), and CABB ($Cs_2AgBiBr_6$) grown *in situ* in a mesoporous titania (M-Ti) framework for efficient CO_2 reduction reaction.[109] The combination of BHP and M-Ti led to the remarkable CH_4 production rates of 32.9 μmol g^{-1} h^{-1} and selectivity of 88.7% (Fig. 9a and d). This is the highest photoreduction rate of CO_2 to CH_4 for BHP nanomaterials among the known reports so far. The photocatalytic activity of these heterojunctions hardly decreased after five cycles, and the production rates of CO and CH_4 remained constant (Fig. 9b, c, e and f). Moreover, no significant changes were observed in other characterizations (XRD, TEM, EDX mapping), indicating the high stability of BHP@M-Ti heterojunctions. *In situ* XPS (Fig. 9g–i) revealed the interfacial charge-transfer pathway of CBB@M-Ti under light. This result proved that the inner surface built-in electric field between the perovskite nanodots and mesoporous titania channels can efficiently promote photoinduced charge transfer (Fig. 9j). Moreover, the micromorphology of the titania frameworks with mesopores (specific surface area of 39.4 m^2 g^{-1},

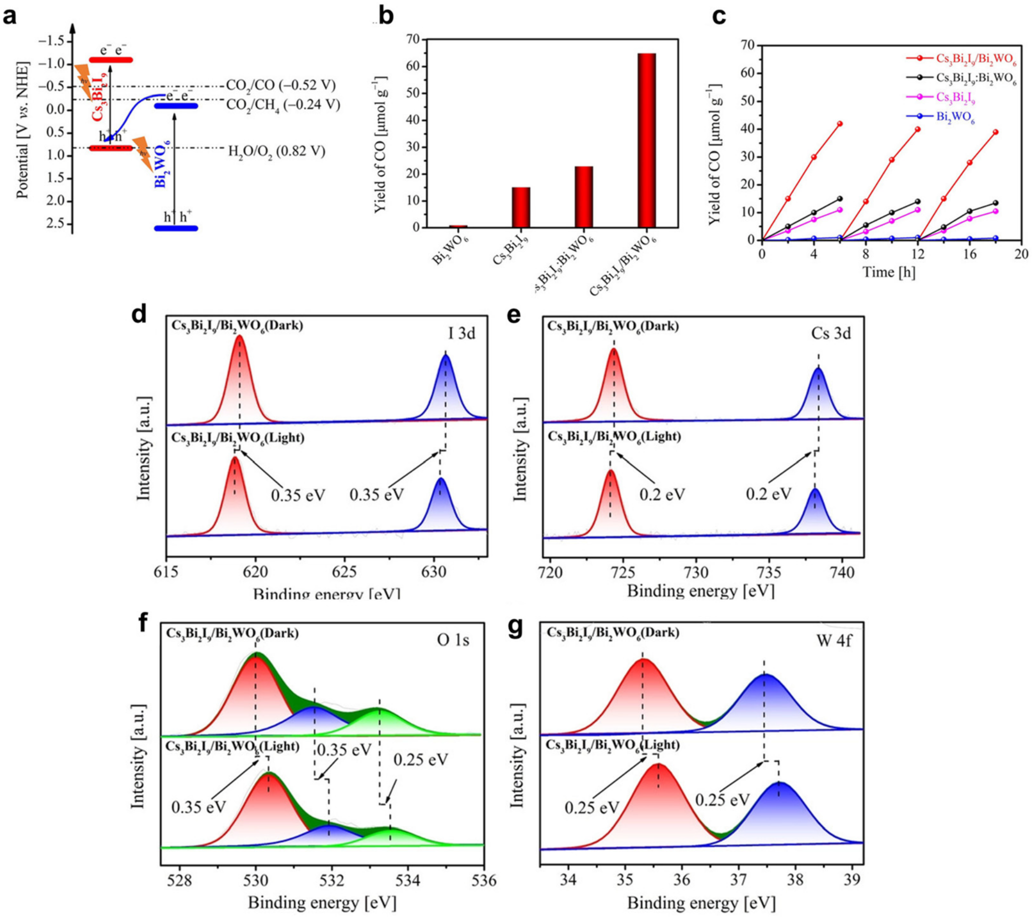

Fig. 8 (a) The band structures for $Cs_3Bi_2I_9$ and Bi_2WO_6. (b) The yield of CO generated from photocatalytic CO_2 reduction after 9 h of irradiation. (c) Recycling stability tests of as-prepared samples with three cycles. (d–g) High-resolution XPS spectra of $Cs_3Bi_2I_9/Bi_2WO_6$ in the dark or under 300 W Xe lamp irradiation with a 400 nm filter: (d) I 3d, (e) Cs 3d, (f) O 1s, and (g) W 4f. Reproduced with permission from ref. 42. Copyright 2021 Wiley-VCH.

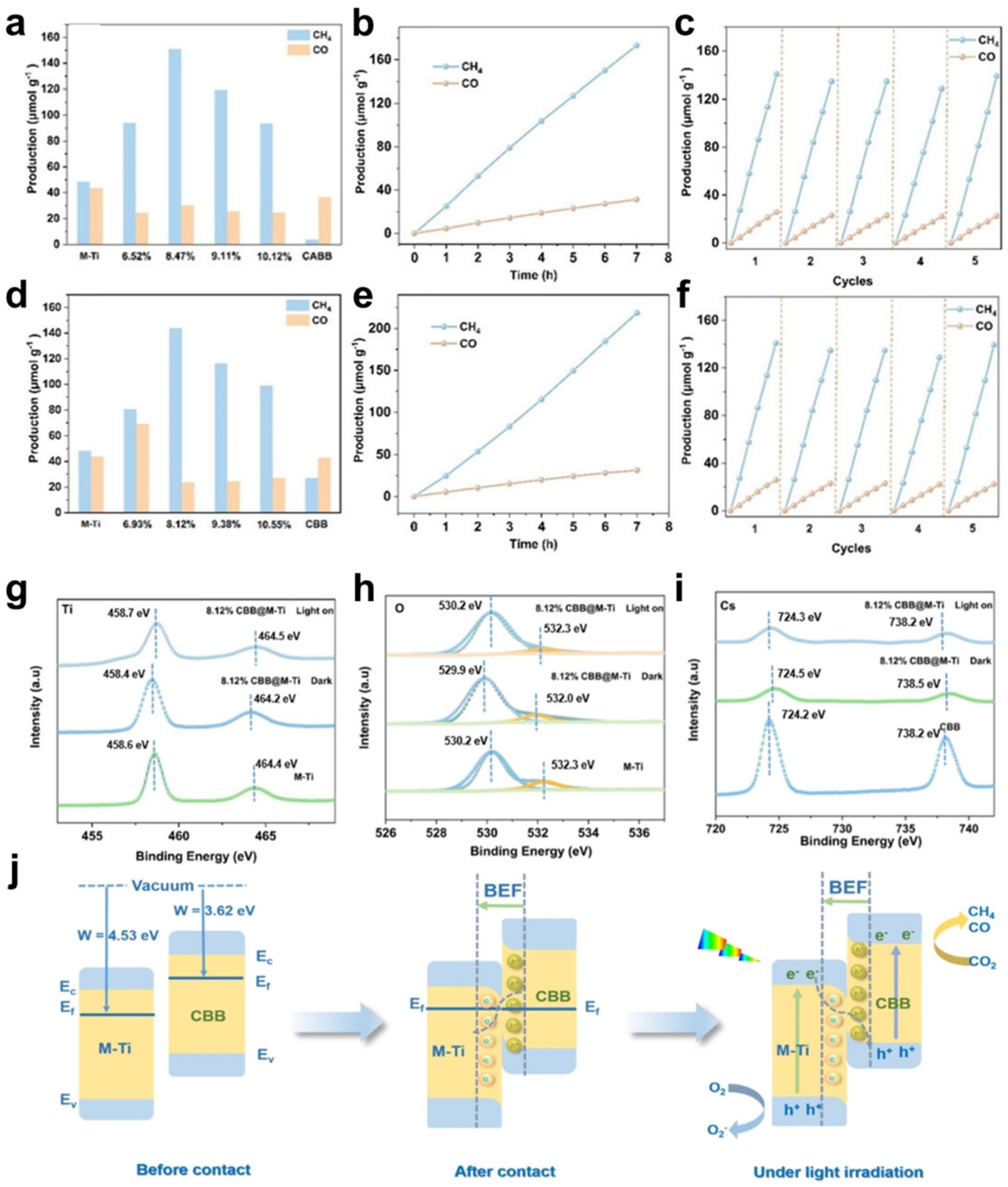

Fig. 9 Photocatalytic yield of CH_4 and CO in five hours over (a) *X*% $Cs_2AgBiBr_6$@M-Ti and (d) *X*% $Cs_3Bi_2Br_9$@M-Ti. Time-dependent production of CH_4 and CO over (b) 8.47% $Cs_2AgBiBr_6$ @M-Ti and (e) 8.12% $Cs_3Bi_2Br_9$@M-Ti. Cycling photocatalysis performance of (c) 8.47% $Cs_2AgBiBr_6$@M-Ti and (f) 8.12% $Cs_3Bi_2Br_9$@M-Ti. High-resolution XPS spectra of Ti 2p (g), O 1s (h), and Cs 3d (i) of 8.12% CBB@M-Ti. (j) Charge transfer mechanism of perovskite@M-Ti under illumination (CBB short for $Cs_3Bi_2Br_9$). Reproduced with permission from ref. 109. Copyright 2022 Wiley-VCH.

pore size of 13.6 nm, and pore volume of 0.134 cm^3 g^{-1}) gave it excellent CO_2 enrichment ability (with a CO_2 uptake of 3.4 cm^3 g^{-1}), which benefits photocatalytic CO_2 reduction with higher reactant concentrations. Meanwhile, the electron-rich perovskite phase with the nanodot shape can afford abundant active centers to smoothly transfer plenty of electrons for CO_2 reduction. Thus, the combination of these nanostructures gives rise to the high methane production rate. Additionally, combination with other semiconductors (*e.g.*, C_3N_4, Sr_2FeNbO_6, In_4SnS_8, $Ti_3C_2T_x$) also promoted the CO_2 conversion rates in photoreduction.[89,112,114,115] There is no doubt that the construction of heterojunctions is a feasible and effective way to improve photocatalytic performance by modulating charge transport.

On the whole, the applications of several BHP photocatalysts in CO_2 photoreduction have been well illustrated with measurable activity and high stability. However, the low efficiency and poor selectivity toward valued hydrocarbons (*e.g.*, CH_4 and C_2H_6) in CO_2 photoreduction should be improved *via* constructing more efficient perovskite photocatalysts. Moreover, the transformation of CO_2 to more valuable oxygenated chemicals such as methanol and formic acid by use of BHP photocatalysts is still unavailable, which requires more investigation. Considering low-level activity in CO_2

photoreduction, another significant concern is how to acquire reliable data with accurate and strict operation during the evaluation of photocatalytic systems. Avoiding the usage of organic solvents/additives, ensuring the cleanliness of photocatalysts, and conducting isotopic labeling tests may be good options to identify whether external carbonaceous contamination exists.

4.3 Organic synthesis

In the past three years, BHP materials have provided promising applications in heterogeneous photocatalytic organic synthesis. Table 4 summarizes recent photocatalytic organic reactions over BHPs materials, including ring-opening reactions, oxidizing reaction and C–H bond activation. In 2019, Dai *et al.* reported that $Cs_3Bi_2Br_9$ nanoparticles could catalyze ring-opening alcoholysis reactions of various epoxides under visible light, which is the first case of employing BHP photocatalysts for organic synthesis.[49] This photocatalytic system not only avoided the utilization of strong acids but also exhibited high activity and good selectivity for epoxide alcoholysis. Moreover, the surface acidity characterization and control experiments have demonstrated that the superior catalytic properties of this BHP photocatalyst originated from suitable acidic sites, which are absent in lead-based perovskites. These acidic sites could activate the epoxides, facilitating further ring-opening reactions.

Moreover, in photocatalytic selective oxidation reactions, BHPs have the capability to activate inert $C(sp^3)$–H bonds. Dai *et al.* designed a confined growth strategy by use of the mesoporous channels of SBA-15 silica, leading to the successful loading of uniform and highly dispersed small $Cs_3Bi_2Br_9$ nanoparticles (2–5 nm).[133] This $Cs_3Bi_2Br_9$/SBA-15-supported photocatalyst could efficiently oxidize hydrocarbons (C5–C16, including aromatic and aliphatic alkanes) under visible light with a conversion rate up to 32 900 μmol g_{cat}^{-1} h^{-1} and excellent selectivity towards aldehydes/ketones (>99%) (Fig. 10a–c). In comparison with the bulk sample, $Cs_3Bi_2Br_9$ nanoparticles with small size can generate rich under-coordinated bismuth sites on the surface ($BiBr_3$ and $BiBi_5$ motifs), which promote the adsorption of hydrocarbons *via* electronic interactions to facilitate the activation of C–H bonds. Furthermore, the smaller perovskite nanoparticles can exhibit shorter diffusion distance of charges in excited states to suppress the charge recombination, boosting the final photocatalytic performance. As the reaction proceeded, the water produced led to the formation of BiOBr, which deactivated the catalyst with totally inhibited photocatalytic performance after 8 h irradiation (Fig. 10c). This deactivation of the photocatalysts can be figured out after the addition of anhydrous Na_2SO_4 (Fig. 10c), which can adsorb water to control the reaction environment with a low-level water content. Another effective strategy for enhancing stability is the fabrication of 2D $Cs_3Bi_2Br_9$ nanoplatelets (a basal size of 2–10 μm and a thickness of ~100 nm),[87] which exhibit more grid crystal framework and fewer surface defects in comparison with the fragile 0D perovskite nanoparticles.

Based on the control tests with different scavengers (Fig. 10d) and *in situ* diffuse reflectance infrared Fourier transform spectroscopy (DRIFTs) (Fig. 10e), the reaction pathway has been proposed with under-coordinated bismuth metal sites and Br anions playing the key roles (Fig. 10f). Under visible light irradiation, the photoinduced electrons and holes were generated from $Cs_3Bi_2Br_9$ nanoparticles. Subsequently, the holes cleaved C–H bonds to produce alkyl radical intermediates ($R^•$), which further formed ROOH intermediates in the presence of electrons and O_2 (Fig. 10g). Moreover, the oxidation sites (Br atoms) on the perovskite surface were in close proximity to the H atoms of hydrocarbon substrates (2.9 Å) due to their unique adsorption at bismuth metal sites, promoting the subsequent selective oxidation of the $C(sp^3)$–H bonds (Fig. 10h).

Later, Shi *et al.* designed and fabricated an antimony-doped BHP $Cs_3Sb_xBi_{2-x}Br_9$ ($0 \le x \le 2$).[155] The addition of Sb broke the local symmetry and made the charges more dispersed, which facilitated the separation and transfer of charges. The simultaneous asymmetric charge distribution enhanced the

Table 4 Summary of recent photocatalytic organic reactions over BHP materials

Catalyst	Solution	Reaction types	Light source	Performance	Ref.
$Cs_3Bi_2Br_9$	Isopropanol	Ring-opening reactions	300 W Xe-lamp ($\lambda \ge 420$ nm)	1333 μmol g^{-1} h^{-1}	49
$Cs_2AgBiBr_6$	Acetonitrile	Oxidation of vanillyl alcohol	White light LED lamp	Conversion: 95%	152
$Cs_3(Bi_xSb_{1-x})_2Br_9$	*n*-Hexane	Oxidation of thioanisole	300 W Xe-lamp ($\lambda \ge 420$ nm)	Conversion: 95%; selectivity: 99%	153
$Cs_3Bi_2I_9/TiO_2$	Aqueous solution	Oxidation of MeOH	M455L3 (blue LED 455 nm)	105 μmol h^{-1}	154
$Cs_3Bi_2Br_9$/SBA-15	Toluene	C–H bond activation	300 W Xe-lamp ($\lambda \ge 420$ nm)	12.6 mmol g_{cat}^{-1} h^{-1} (90% selectivity)	133
$Cs_3Sb_xBi_{2-x}Br_9$ ($0 \le x \le 2$)	Acetonitrile/ toluene	C–H bond activation	White light LED lamp	~26 μmol h^{-1}	155
$Cs_3Bi_2Br_9/TiO_2$	Isopropanol	C–H bond activation	300 W Xe-lamp ($\lambda \ge 420$ nm)	1465 μmol g^{-1} h^{-1}	156
$Cs_3Bi_2Br_9$/CdS	Toluene	C–H bond activation	300 W Xe-lamp ($\lambda \ge 420$ nm)	6.79 mmol g^{-1} h^{-1}	113
$Cs_3Bi_2Br_9/Ti_3C_2T_x$	Toluene	C–H bond activation	5 W LED	2121μmol g^{-1} h^{-1} (100% selectivity)	107
$Cs_3Bi_2Br_9$/d-BiOBr	Toluene	C–H bond activation	300 W Xe-lamp ($\lambda \ge 420$ nm)	7.24 mmol g^{-1} h^{-1}	108
$Cs_3Bi_2Br_9/g\text{-}C_3N_4$	Toluene	C–H bond activation	300 W Xe-lamp ($\lambda \ge 400$ nm, 500 mW cm^{-2})	4.53 mmol g^{-1} h^{-1}	157

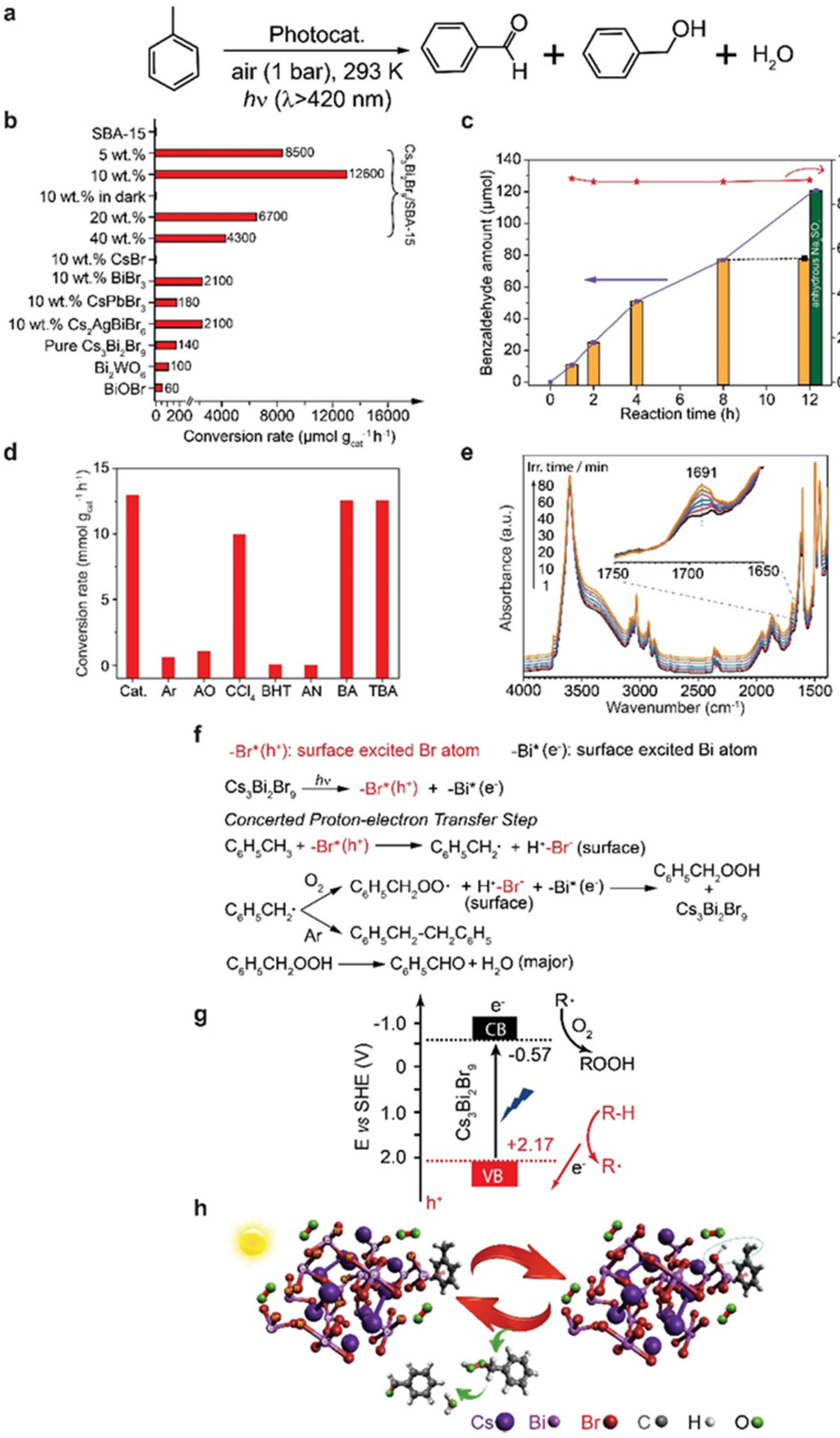

Fig. 10 (a) The reaction formula of photocatalytic toluene oxidation. (b) The toluene conversion rate over different photocatalysts. (c) The time dependence of toluene photooxidation over 10 wt% $Cs_3Bi_2Br_9$/SBA-15. (d) Control tests in the anaerobic condition or with different scavengers. (e) *In situ* DRIFTs spectra of $Cs_3Bi_2Br_9$/SBA-15 sample exposed to the gas mixture of O_2 and toluene under light irradiation. (f) Possible reaction pathways for the photooxidation of toluene, involving the concerted proton–electron transfer process. (g) The band structure of $Cs_3Bi_2Br_9$ nanoparticles, including the proposed redox reaction paths by use of electrons and holes. (h) The possible photocatalytic mechanism of the hydrocarbon oxidation over $Cs_3Bi_2Br_9$ nanoparticles under visible light irradiation in air. The blue elliptic mark indicates the production of a benzyl radical intermediate after cleaving the C–H bond. Reproduced with permission from ref. 133. Copyright 2020 Wiley-VCH.

adsorption of toluene. It effectively reduced the activation energy barrier of C–H bond, which improved the reaction efficiency. Besides, Estrada-Pomares *et al.* reported that $Cs_2AgBiBr_6$ and $Cs_3Bi_2Br_9$ were able to efficiently and stably oxidize vanillyl alcohol to vanillin under visible light with a conversion rate of 95%.[152] Mechanistic investigations have shown that photogenerated holes and superoxide radicals from the reduction of O_2 by electrons mainly contributed to the oxidation of vanillyl alcohol. In addition, some composite materials such as $Cs_3Bi_2Br_9$-TiO_2 or -BiOBr or -CdS or -$Ti_3C_2T_x$ or -C_3N_4 have been successfully applied in C–H bond activation with improved photocatalytic performance, especially for the oxidation of toluene.[107,108,113,156,157]

The complexity and diversity of photocatalytic reaction mechanisms bring the research of BHP photocatalysts in organic synthesis huge challenges and difficulties. More efficient, robust and well-matched BHP photocatalyst nanomaterials should be designed and prepared to drive significant organic transformations under visible light, which can generate value-added products in a green and sustainable way. Even though the photocatalytic organic synthesis reactions over BHP photocatalysts are still in their infancy at the present point, the BHP-based photocatalytic systems have shown highly promising potential, playing important roles in the future artificial photosynthesis field.

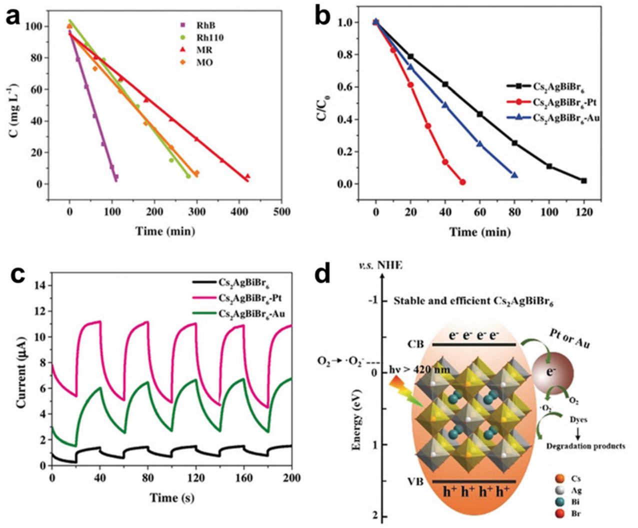

Fig. 11 (a) Kinetic curves of the RhB (pink curve), Rh110 (green curve), MR (red curve), and MO (orange curve) degradation fitted using a pseudo-zeroth-order reaction model. (b) Plots of C/C_0 *versus* the irradiation time for the photodegradation of RhB in the presence of $Cs_2AgBiBr_6$, $Cs_2AgBiBr_6$-Pt, and $Cs_2AgBiBr_6$-Au. (c) Photocurrent response of $Cs_2AgBiBr_6$, $Cs_2AgBiBr_6$-Pt, and $Cs_2AgBiBr_6$-Au. (d) The proposed photocatalytic degradational mechanism of dyes by $Cs_2AgBiBr_6$. Reproduced with permission from ref. 47. Copyright 2019 Wiley-VCH.

4.4 Organic pollutant degradation

The photocatalytic advanced oxidation process for the purification of wastewater with various organic contaminants has attracted increasing attention,[115] and presents a few merits such as mild reaction conditions, powerful oxidation ability and low-cost treatment.[158] Recently, BHPs have been reported as remarkable photocatalysts in the treatment of wastewater and air pollutants (such as NO).[111,159] For example, the $(CH_3NH_3)_3Bi_2I_9$ nanomaterial has been applied in cleaning simulated industrial wastewater with a high photodegradation activity for both fluorescent dye (rhodamine B) and thiazine dye (methylene blue) under visible light.[134] However, the aqueous environment can lead to the hydrolysis of $(CH_3NH_3)_3Bi_2I_9$ easily. Thus, the real photocatalytic species in this work is still uncertain, since the formed BiOI phase from hydrolysis of BHP can present decent activity for the photodegradation of dyes as well.[160]

Impressively, the $Cs_2AgBiBr_6$ double perovskite material exhibited excellent activity (almost complete degradation) toward a few organic dyes, including rhodamine B (RhB), rhodamine 110 (RH110), methyl red (MR), and methyl orange (MO) (Fig. 11a).[47] The excellent activities were probably ascribable to the unique surface Ag or Bi sites on $Cs_2AgBiBr_6$, facilitating the activation of O_2 or dyes. Furthermore, the photocatalytic degradation activity could be dramatically promoted with the deposition of Pt or Au as co-catalysts (Fig. 11b). The stability of $Cs_2AgBiBr_6$ photocatalysts could be maintained within 5 cycles of reactions, which is consistent with the photocurrent response (Fig. 11c). However, if more cycling tests were performed, the produced water might lead to partial degradation of $Cs_2AgBiBr_6$ *via* hydrolysis, which would inevitably lead to deactivation of perovskites. As shown in Fig. 11d, the proposed photodegradation mechanism revealed that the dye molecules underwent a complete mineralization process, where the main active species came from the superoxide radical ($^{\bullet}O_2^-$). Additionally, the solvent using ethanol instead of water ensured the high temporary stability of $Cs_2AgBiBr_6$ photocatalysts. Otherwise, the common hydrolysis issue of BHPs would take place as well. The presence of alcohol solvent may lead to the undesired oxidation of ethanol to aldehydes, suggesting the waste of photoinduced charges. Besides, the products from the mineralization of dyes include water, which indicates the inevitable existence of a hydrolysis problem if abundant dyes are decomposed. In 2020, Bresolin *et al.* confirmed the advantage of composited heterojunctions in photocatalytic degradation.[110] They fabricated $Cs_3Bi_2I_9$/g-C_3N_4 heterojunctions through a facile electrostatic assembly method. The $Cs_3Bi_2I_9$/g-C_3N_4 composites showed the better stability and an outstanding yield for photocatalytic degradation of organic compound (RhB, MB, MO) in water solution under visible light irradiation.

On the whole, these research works illustrate the broad prospects and significance of BHP nanomaterials in photocatalytic organic pollution degradation. However, the photocatalytic activities of BHP photocatalysts in practical industrial wastewater with quite complicated composition are still unclear, which deserves more thorough investigations, especially in the neutral or basic aqueous solutions. Besides, the photocatalytic degradation of persistent organic pollutant (POPs) and plastic polymers has already been realized by some bismuth-based photocatalysts (such as $BiOBr/Fe_3O_4$ nanocomposites[161] and BiOCl nanoflowers[162]) with good activity. The decent remediation performance mainly comes from the generation of powerful hydroxyl radicals or holes by these bismuth-based nanomaterials under visible light irradiation. Thus, BHPs with bismuth as the metal center, possessing diverse compositions and electronic structures, may be promising candidates for the photocatalytic degradation of POPs and polymers. This deserves more scientific investigations in the future.

4.5 Other photocatalytic reaction

Photocatalytic approaches have been applied in various fields, where photoinduced polymerization has attracted much attention due to the mild conditions, low cost and high efficiency.[163] Some frequently used photocatalysts always involve expensive transition metal compounds and toxic organic initiators, leading to burdens on the environment and the economy. Recently, some BHP nanomaterials-based photocatalytic systems have been successfully designed for photoinduced polymerization.[135,136]

Zhu *et al.* have *in situ* embedded $MA_3Bi_2Br_9$ NCs in the hydrophobic COFs matrix for successful photocatalytic applications in both water and organic solvents.[135] Firstly, $BiBr_3$ was dissolved in TAPT-DMTA COF precursor solution. After the addition of MABr solution, $MA_3Bi_2Br_9$ was generated *in situ* on the COFs (Fig. 12a and b). This nanocomposite demonstrated outstanding photocatalytic performance for photopolymerization in both organic and aqueous phases, yielding oligo-(ethylene glycol) methyl ether acrylate (OEGMEA) polymer with a Mn of 22.7 kDa and $Đ$ of 1.27 (Fig. 12c). The added co-initiator MPA (or carboxylic acids) was activated by the hole generated from $MA_3Bi_2Br_9$ under visible light to produce thiyl or alkyl free radicals. These active radicals could initiate chain polymerization though the chain transfer process. However, these polymerizations were difficult to control in a precise way. Moreover, the absence of COFs led to no activity towards polymerization, since the $MA_3Bi_2Br_9$ perovskites were quickly degraded into white BiOBr phase in water. Thus, the water-resisting COF porous shells can efficiently protect perovskite nanocrystals from attack by H_2O molecules, resulting in smooth photoinduced polymerization. Besides, this protection effect can ensure the reusability of $MA_3Bi_2Br_9$-COFs nanocomposites for at least four cycles without an obvious decease in the final conversion of monomers. On the whole, both the powerful oxidation ability from photoinduced holes and hydrophobic encapsulation of COF shells in the $MA_3Bi_2Br_9$-COF system can lead to photopolymerization with excellent performance and stability in water and organic phases.

Additionally, some other important photocatalytic reactions such as O_2 evolution and H_2O_2 generation have been well

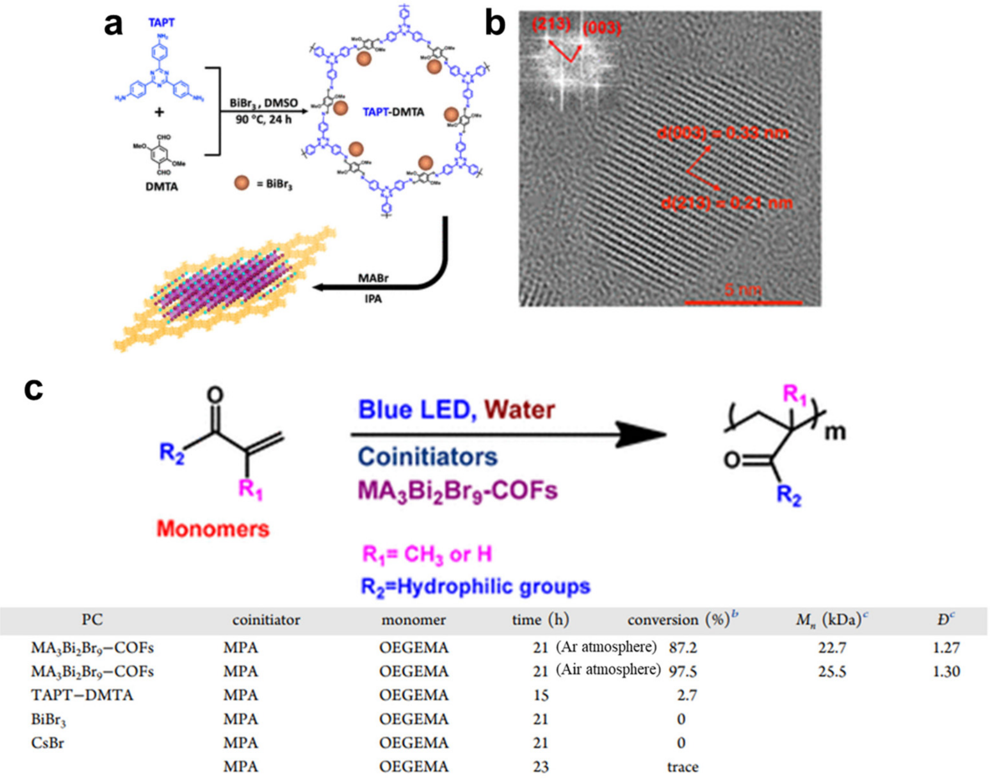

PC	coinitiator	monomer	time (h)	conversion (%)[b]	M_n (kDa)[c]	$Đ$[c]
$MA_3Bi_2Br_9$–COFs	MPA	OEGEMA	21 (Ar atmosphere)	87.2	22.7	1.27
$MA_3Bi_2Br_9$–COFs	MPA	OEGEMA	21 (Air atmosphere)	97.5	25.5	1.30
TAPT–DMTA	MPA	OEGEMA	15	2.7		
$BiBr_3$	MPA	OEGEMA	21	0		
CsBr	MPA	OEGEMA	21	0		
	MPA	OEGEMA	23	trace		

Fig. 12 (a) The *in situ* synthetic protocol for $MA_3Bi_2Br_9$-COFs nanocomposites. (b) The HRTEM image indicating the formation of $MA_3Bi_2Br_9$ NCs-COFs nanocomposites; inserted graph: FFT pattern of the selected area. (c) Partial results of photoinduced polymerization reactions using $MA_3Bi_2Br_9$-COFs nanocomposites in water. Reproduced with permission from ref. 135. Copyright 2022 American Chemical Society.

investigated by the use of efficient photocatalysts.[52,164] Although the application of BHP nanomaterials on these reactions is still unclear, the establishment of BHP-based photocatalytic systems with high stability in water phase and essential active sites could be promising candidates.

5. Conclusion and outlook

In conclusion, the recent progress in the synthesis and photocatalytic applications of BHP nanomaterials with diverse structures and their physical–chemical properties has been reviewed. The preparation of BHP nanomaterials with different dimensions in morphology (0D, 2D and heterostructures) can utilize several chemical wet approaches, including antisolvent, hot-injection, ion-exchange reactions, physical exfoliation and rapid cooling recrystallization. The fabricated BHP nanomaterials can present diverse nanostructures, such as 0D quantum dots, 2D nanosheets and hetero-junctions (*e.g.*, Z-type 2D $Cs_3Bi_2I_9$/2D CeO_2). Moreover, the changes of halide anions or the introduction of Ag/Cu heteroatoms can facilely regulate the band structures with bandgaps varying from 1.8 to 3.1 eV, which can offer tunable optoelectronic properties. Besides, the construction of heterojunctions (*e.g.*, Schottky, type II, and Z-scheme junctions) by combining BHPs with other semiconductors or metals results in improved charge separation/transport and rich catalytically active sites on the surface, which help to drive desired redox reactions with higher efficiencies. Regarding photocatalytic applications, the established BHP photocatalysts have shown decent photocatalytic activity and stability in several reactions, including H_2 generation, CO_2 reduction, organic synthesis and pollutant degradation. However, the quantum yields and selectivity control over BHP-based photocatalytic systems still locate at a low level. Thus, it is urgent to design and prepare more efficient BHP photocatalysts with aligned active sites on the surface and promoted charge transport/separation. Another main issue lies in the stability of BHP nanomaterials in the environment containing H_2O molecules, which severely hinders their application for pure water splitting or organic oxidations in aerobic conditions. Regarding the photocatalytic mechanisms over BHP photocatalysts, the nature of real active sites, the key reaction paths containing rate-determining steps, and the whole solar-to-chemical energy process are still unclear for most reported photocatalytic systems.

Finally, in our opinion, future research directions for BHPs in photocatalysis may involve: (1) the fabrication of novel BHPs with diverse nanostructures and elemental compositions. For instance, 1D linear or 3D porous nanomaterials like inverse-opal crystals are still unreported. The replacement of A or B-site atoms by other species, such as Cu_2AgBiX_6 and Cs_2InBiX_6, may provide unique catalytically active sites; (2) the surface engineering on BHP photocatalysts. For example, the creation of bismuth or halide vacancy sites could vary the optical properties and surface chemical environment. The doping of heteroatoms (*e.g.*, Mn, Eu, Sn, Sb, and In) on the surface may modulate the electronic structures with suitable sub-states and offer diverse adsorption sites for certain reactants. Besides, the surface environment of BHPs can be modified as well by bridging organic ligands, or depositing co-catalysts such as metal nanoparticles or metal complexes; (3) the establishment of effective heterojunctions. By introducing other semiconductors or plasmonic metals, the nanocomposites may present promoted photocatalytic properties with improved charge diffusion and desired active sites. Furthermore, the nanostructures of these composites are crucial for their physical–chemical properties as well. For instance, the core–shell architecture with inert shells (*e.g.*, TiO_2, CdS, and metal–organic frameworks) toward water may provide high moisture stability; (4) discovering more matched redox reactions in the field of photocatalytic organic synthesis. Through an in-depth understanding of the surface chemical environment in BHP photocatalysts, more organic reactions with high economy should be screened out in a rational and efficient way. For the organic reactions easily and safely realized by conventional thermal catalytic methods (*e.g.*, reaction temperature T_r < 150 °C and ambient pressure) with high activities and selectivity, they are not the most desired target reactions. In contrast, challenging reactions always require harsh reaction conditions (*e.g.*, $T_r \geq 350$ °C, reaction pressure $P_r \geq 5$ MPa), which should be targeted, such as the direct dehydrogenation of butane (usually $T_r \geq 600$ °C). (5) Theoretical predications *via* artificial intelligence (AI). Powerful AI techniques such as machine learning and deep learning could build the material models to predict the optimal composition in BHPs by a high-throughput computational approach. This not only provides diverse design pathways, but also saves abundant time for researchers. This may guide the fabrication of next-generation BHPs with high stability and activity for photocatalysis.

Conflicts of interest

The authors declare no potential conflicts of interest.

Acknowledgements

This work was supported by the National Natural Science Foundation of China (NSFC) (No. 22205230, 21725102 and 91961106), Youth Fund Project of Natural Science Foundation of Jiangsu Province (No. BK20220287), Gusu Innovation and Entrepreneurship Leading Talents Program (No. ZXL2022468), startup grant from the University of Science and Technology of China (USTC) (No. KY2260080010). The authors thank Xuesen Liu (Intermediate Engineer) and Zhibin Li (Intermediate Engineer) from Failure Analysis Laboratory company (FALAB) for the thorough discussions during the halide perovskite project cooperation.

References

1 A. Fujishima and K. Honda, *Nature*, 1972, **238**, 37–38.

2 A. Kudo and Y. Miseki, *Chem. Soc. Rev.*, 2009, **38**, 253–278.

3 Y. Dai, Q. Bu, R. Sooriyagoda, P. Tavadze, O. Pavlic, T. Lim, Y. Shen, A. Mamakhel, X. Wang, Y. Li, H. Niemantsverdriet, B. B. Iversen, F. Besenbacher, T. Xie, J. P. Lewis, A. D. Bristow, N. Lock and R. Su, *J. Phys. Chem. Lett.*, 2019, **10**, 5381–5386.

4 Y. Liu, X. Zhang, L. Lu, J. Ye, J. Wang, X. Li, X. Bai and W. Wang, *Chin. Chem. Lett.*, 2022, **33**, 1271–1274.

5 X. Li, Y. Sun, J. Xu, Y. Shao, J. Wu, X. Xu, Y. Pan, H. Ju, J. Zhu and Y. Xie, *Nat. Energy*, 2019, **4**, 690–699.

6 F. Xu, K. Meng, B. Cheng, S. Wang, J. Xu and J. Yu, *Nat. Commun.*, 2020, **11**, 4613.

7 L. Shi, Y. Shi, S. Zhuo, C. Zhang, Y. Aldrees, S. Aleid and P. Wang, *Nano Energy*, 2019, **60**, 222–230.

8 R. Yang, S. Zhong, L. Zhang and B. Liu, *Sep. Purif. Technol.*, 2020, **235**, 116270.

9 H. Cheng and W. Xu, *Org. Biomol. Chem.*, 2019, **17**, 9977–9989.

10 S. Gisbertz and B. Pieber, *ChemPhotoChem*, 2020, **4**, 456–475.

11 Y. Dai and Y. Xiong, *Nano Res. Energy*, 2022, **1**, e9120006.

12 H. Tan, P. Kong, R. Zhang, M. Gao, M. Liu, X. Gu, W. Liu and Z. Zheng, *The Innovation*, 2021, **2**, 100089.

13 H. L. Tan, F. F. Abdi and Y. H. Ng, *Chem. Soc. Rev.*, 2019, **48**, 1255–1271.

14 N. Zhang, S. Liu and Y.-J. Xu, *Nanoscale*, 2012, **4**, 2227–2238.

15 S. C. Shit, I. Shown, R. Paul, K.-H. Chen, J. Mondal and L.-C. Chen, *Nanoscale*, 2020, **12**, 23301–23332.

16 J. Lee, L.-L. Tan and S.-P. Chai, *Nanoscale*, 2021, **13**, 7011–7033.

17 G. Zhao and X. Xu, *Nanoscale*, 2021, **13**, 10649–10667.

18 G. Xing, N. Mathews, S. S. Lim, N. Yantara, X. Liu, D. Sabba, M. Grätzel, S. Mhaisalkar and T. C. Sum, *Nat. Mater.*, 2014, **13**, 476–480.

19 L. Protesescu, S. Yakunin, M. I. Bodnarchuk, F. Krieg, R. Caputo, C. H. Hendon, R. X. Yang, A. Walsh and M. V. Kovalenko, *Nano Lett.*, 2015, **15**, 3692–3696.

20 F. Zhang, H. Zhong, C. Chen, X.-G. Wu, X. Hu, H. Huang, J. Han, B. Zou and Y. Dong, *ACS Nano*, 2015, **9**, 4533–4542.

21 Q. Zhang, R. Su, X. Liu, J. Xing, T. C. Sum and Q. Xiong, *Adv. Funct. Mater.*, 2016, **26**, 6238–6245.

22 W.-L. Hong, Y.-C. Huang, C.-Y. Chang, Z.-C. Zhang, H.-R. Tsai, N.-Y. Chang and Y.-C. Chao, *Adv. Mater.*, 2016, **28**, 8029–8036.

23 Y. Fu, H. Zhu, A. W. Schrader, D. Liang, Q. Ding, P. Joshi, L. Hwang, X. Y. Zhu and S. Jin, *Nano Lett.*, 2016, **16**, 1000–1008.

24 S. D. Stranks, G. E. Eperon, G. Grancini, C. Menelaou, M. J. P. Alcocer, T. Leijtens, L. M. Herz, A. Petrozza and H. J. Snaith, *Science*, 2013, **342**, 341–344.

25 C. Wehrenfennig, G. E. Eperon, M. B. Johnston, H. J. Snaith and L. M. Herz, *Adv. Mater.*, 2014, **26**, 1584–1589.

26 D. Shi, V. Adinolfi, R. Comin, M. Yuan, E. Alarousu, A. Buin, Y. Chen, S. Hoogland, A. Rothenberger, K. Katsiev, Y. Losovyj, X. Zhang, P. A. Dowben, O. F. Mohammed, E. H. Sargent and O. M. Bakr, *Science*, 2015, **347**, 519–522.

27 T. M. Brenner, D. A. Egger, L. Kronik, G. Hodes and D. Cahen, *Nat. Rev. Mater.*, 2016, **1**, 15007.

28 S.-T. Ha, R. Su, J. Xing, Q. Zhang and Q. Xiong, *Chem. Sci.*, 2017, **8**, 2522–2536.

29 K. Chen, S. Schünemann, S. Song and H. Tüysüz, *Chem. Soc. Rev.*, 2018, **47**, 7045–7077.

30 J. Yuan, H. Liu, S. Wang and X. Li, *Nanoscale*, 2021, **13**, 10281–10304.

31 H. L. Wells, *Am. J. Sci.*, 1893, **45**, 121.

32 A. Kojima, K. Teshima, Y. Shirai and T. Miyasaka, *J. Am. Chem. Soc.*, 2009, **131**, 6050–6051.

33 J. Sun, J. Wu, X. Tong, F. Lin, Y. Wang and Z. M. Wang, *Adv. Sci.*, 2018, **5**, 1700780.

34 P. Chen, W.-J. Ong, Z. Shi, X. Zhao and N. Li, *Adv. Funct. Mater.*, 2020, **30**, 1909667.

35 M. Ren, X. Qian, Y. Chen, T. Wang and Y. Zhao, *J. Hazard. Mater.*, 2022, **426**, 127848.

36 J. Li, H.-L. Cao, W.-B. Jiao, Q. Wang, M. Wei, I. Cantone, J. Lü and A. Abate, *Nat. Commun.*, 2020, **11**, 310.

37 M. Lyu, J.-H. Yun, P. Chen, M. Hao and L. Wang, *Adv. Energy Mater.*, 2017, **7**, 1602512.

38 Q. Fan, G. V. Biesold-McGee, J. Ma, Q. Xu, S. Pan, J. Peng and Z. Lin, *Angew. Chem., Int. Ed.*, 2020, **59**, 1030–1046.

39 J. Li, J. Duan, X. Yang, Y. Duan, P. Yang and Q. Tang, *Nano Energy*, 2021, **80**, 105526.

40 H. Fu, *Sol. Energy Mater. Sol. Cells*, 2019, **193**, 107–132.

41 M. Wang, W. Wang, B. Ma, W. Shen, L. Liu, K. Cao, S. Chen and W. Huang, *Nano-Micro Lett.*, 2021, **13**, 62.

42 Z.-L. Liu, R.-R. Liu, Y.-F. Mu, Y.-X. Feng, G.-X. Dong, M. Zhang and T.-B. Lu, *Sol. RRL*, 2021, **5**, 2000691.

43 H. Tang, Y. Xu, X. Hu, Q. Hu, T. Chen, W. Jiang, L. Wang and W. Jiang, *Adv. Sci.*, 2021, **8**, 2004118.

44 J. Pascual, G. Nasti, M. H. Aldamasy, J. A. Smith, M. Flatken, N. Phung, D. Di Girolamo, S.-H. Turren-Cruz, M. Li, A. Dallmann, R. Avolio and A. Abate, *Mater. Adv.*, 2020, **1**, 1066–1070.

45 Y. Guo, G. Liu, Z. Li, Y. Lou, J. Chen and Y. Zhao, *ACS Sustainable Chem. Eng.*, 2019, **7**, 15080–15085.

46 G.-N. Liu, R.-Y. Zhao, B. Xu, Y. Sun, X.-M. Jiang, X. Hu and C. Li, *ACS Appl. Mater. Interfaces*, 2020, **12**, 54694–54702.

47 Z. Zhang, Y. Liang, H. Huang, X. Liu, Q. Li, L. Chen and D. Xu, *Angew. Chem., Int. Ed.*, 2019, **58**, 7263–7267.

48 B. Yang, J. Chen, F. Hong, X. Mao, K. Zheng, S. Yang, Y. Li, T. Pullerits, W. Deng and K. Han, *Angew. Chem., Int. Ed.*, 2017, **56**, 12471–12475.

49 Y. Dai and H. Tüysüz, *ChemSusChem*, 2019, **12**, 2587–2592.

50 X. Li, J. Hu, T. Yang, X. Yang, J. Qu and C. M. Li, *Nano Energy*, 2022, **92**, 106714.

51 C. Chen, J. Hu, X. Yang, T. Yang, J. Qu, C. Guo and C. M. Li, *ACS Appl. Mater. Interfaces*, 2021, **13**, 20162–20173.

52 J. Hu, C. Chen, H. Yang, F. Yang, J. Qu, X. Yang, W. Sun, L. Dai and C. M. Li, *Appl. Catal., B*, 2022, **317**, 121723.

53 J. Hu, C. Chen, T. Hu, J. Li, H. Lu, Y. Zheng, X. Yang, C. Guo and C. M. Li, *J. Mater. Chem. A*, 2020, **8**, 19484–19492.

54 J. Hu, C. Chen, Y. Zheng, G. Zhang, C. Guo and C. M. Li, *Small*, 2020, **16**, 2002988.

55 J. Hu, D. Chen, Z. Mo, N. Li, Q. Xu, H. Li, J. He, H. Xu and J. Lu, *Angew. Chem., Int. Ed.*, 2019, **58**, 2073–2077.

56 C. B. Hiragond, N. S. Powar and S.-I. In, *Nanomaterials*, 2020, **10**, 2569.

57 C. Han, X. Zhu, J. S. Martin, Y. Lin, S. Spears and Y. Yan, *ChemSusChem*, 2020, **13**, 4005–4025.

58 J. Chen, C. Dong, H. Idriss, O. F. Mohammed and O. M. Bakr, *Adv. Energy Mater.*, 2020, **10**, 1902433.

59 J. Luo, W. Zhang, H. Yang, Q. Fan, F. Xiong, S. Liu, D.-S. Li and B. Liu, *EcoMat*, 2021, **3**, e12079.

60 H. Huang, D. Verhaeghe, B. Weng, B. Ghosh, H. Zhang, J. Hofkens, J. A. Steele and M. B. J. Roeffaers, *Angew. Chem., Int. Ed.*, 2022, **61**, e202203261.

61 K. Ren, S. Yue, C. Li, Z. Fang, K. A. M. Gasem, J. Leszczynski, S. Qu, Z. Wang and M. Fan, *J. Mater. Chem. A*, 2022, **10**, 407–429.

62 Y. Lin, J. Guo, J. San Martin, C. Han, R. Martinez and Y. Yan, *Chem. – Eur. J.*, 2020, **26**, 13118–13136.

63 Y. Zhang, Y. Ma, Y. Wang, X. Zhang, C. Zuo, L. Shen and L. Ding, *Adv. Mater.*, 2021, **33**, 2006691.

64 L. Zhang, K. Wang and B. Zou, *ChemSusChem*, 2019, **12**, 1612–1630.

65 S. Attique, N. Ali, S. Ali, R. Khatoon, N. Li, A. Khesro, S. Rauf, S. Yang and H. Wu, *Adv. Sci.*, 2020, **7**, 1903143.

66 C. Wu, Q. Zhang, G. Liu, Z. Zhang, D. Wang, B. Qu, Z. Chen and L. Xiao, *Adv. Energy Mater.*, 2020, **10**, 1902496.

67 F. Ünlü, M. Deo, S. Mathur, T. Kirchartz and A. Kulkarni, *J. Phys. D: Appl. Phys.*, 2021, **55**, 113002.

68 P. Cheng, K. Han and J. Chen, *ACS Mater. Lett.*, 2023, **5**, 60–78.

69 M. M. Byranvand, C. Otero-Martínez, J. Ye, W. Zuo, L. Manna, M. Saliba, R. L. Z. Hoye and L. Polavarapu, *Adv. Opt. Mater.*, 2022, **10**, 2200423.

70 Y. Tang, C. H. Mak, G. Jia, K.-C. Cheng, J.-J. Kai, C.-W. Hsieh, F. Meng, W. Niu, F.-F. Li, H.-H. Shen, X. Zhu, H. M. Chen and H.-Y. Hsu, *J. Mater. Chem. A*, 2022, **10**, 12296–12316.

71 J. Wu, J. Chen, J. Gao, Z. Chen, L. Li and W. Wang, *Energy Fuels*, 2022, **36**, 14613–14624.

72 M. R. Hoffmann, S. T. Martin, W. Choi and D. W. Bahnemann, *Chem. Rev.*, 1995, **95**, 69–96.

73 B.-M. Bresolin, Y. Park and D. W. Bahnemann, *Catalysts*, 2020, **10**, 709.

74 S. Meloni, G. Palermo, N. Ashari-Astani, M. Grätzel and U. Rothlisberger, *J. Mater. Chem. A*, 2016, **4**, 15997–16002.

75 L. N. Quan, B. P. Rand, R. H. Friend, S. G. Mhaisalkar, T.-W. Lee and E. H. Sargent, *Chem. Rev.*, 2019, **119**, 7444–7477.

76 J. Shamsi, A. S. Urban, M. Imran, L. De Trizio and L. Manna, *Chem. Rev.*, 2019, **119**, 3296–3348.

77 K. K. Bass, L. Estergreen, C. N. Savory, J. Buckeridge, D. O. Scanlon, P. I. Djurovich, S. E. Bradforth, M. E. Thompson and B. C. Melot, *Inorg. Chem.*, 2017, **56**, 42–45.

78 M. Usman and Y. Qingfeng, *Crystals*, 2020, **10**, 62.

79 X.-G. Zhao, D. Yang, J.-C. Ren, Y. Sun, Z. Xiao and L. Zhang, *Joule*, 2018, **2**, 1662–1673.

80 H.-J. Feng, W. Deng, K. Yang, J. Huang and X. C. Zeng, *J. Phys. Chem. C*, 2017, **121**, 4471–4480.

81 A. J. Kale, R. Chaurasiya and A. Dixit, *ACS Appl. Energy Mater.*, 2022, **5**, 10427–10445.

82 M. Y. Leng, Y. Yang, K. Zeng, Z. W. Chen, Z. F. Tan, S. R. Li, J. H. Li, B. Xu, D. B. Li, M. P. Hautzinger, Y. P. Fu, T. Y. Zhai, L. Xu, G. D. Niu, S. Jin and J. Tang, *Adv. Funct. Mater.*, 2018, **28**, 1704446.

83 B. Li, L. Fu, S. Li, H. Li, L. Pan, L. Wang, B. Chang and L. Yin, *J. Mater. Chem. A*, 2019, **7**, 20494–20518.

84 M. Leng, Z. Chen, Y. Yang, Z. Li, K. Zeng, K. Li, G. Niu, Y. He, Q. Zhou and J. Tang, *Angew. Chem., Int. Ed.*, 2016, **55**, 15012–15016.

85 Y. Lou, M. Fang, J. Chen and Y. Zhao, *Chem. Commun.*, 2018, **54**, 3779–3782.

86 J. Sheng, Y. He, J. Li, C. Yuan, H. Huang, S. Wang, Y. Sun, Z. Wang and F. Dong, *ACS Nano*, 2020, **14**, 13103–13114.

87 Y. Dai and H. Tüysüz, *Sol. RRL*, 2021, **5**, 2100265.

88 Y. Tang, C. H. Mak, R. Liu, Z. Wang, L. Ji, H. Song, C. Tan, F. Barrière and H.-Y. Hsu, *Adv. Funct. Mater.*, 2020, **30**, 2006919.

89 Y. Wang, H. Huang, Z. Zhang, C. Wang, Y. Yang, Q. Li and D. Xu, *Appl. Catal., B*, 2021, **282**, 119570.

90 S. S. Bhosale, A. K. Kharade, E. Jokar, A. Fathi, S.-M. Chang and E. W.-G. Diau, *J. Am. Chem. Soc.*, 2019, **141**, 20434–20442.

91 H. Yang, T. Cai, E. Liu, K. Hills-Kimball, J. Gao and O. Chen, *Nano Res.*, 2019, **13**, 282–291.

92 Y. Tang, L. Gomez, M. van der Laan, D. Timmerman, V. Sebastian, C.-C. Huang, T. Gregorkiewicz and P. Schall, *J. Mater. Chem. C*, 2021, **9**, 158–163.

93 R. D. Nelson, K. Santra, Y. Wang, A. Hadi, J. W. Petrich and M. G. Panthani, *Chem. Commun.*, 2018, **54**, 3640–3643.

94 M. Li, S. Xu, L. Wu, H. Tang, B. Zhou, J. Xu, Q. Yang, T. Zhou, Y. Qiu, G. Chen, G. I. N. Waterhouse and K. Yan, *ACS Energy Lett.*, 2022, **7**, 3370–3377.

95 B. Yang, J. Chen, S. Yang, F. Hong, L. Sun, P. Han, T. Pullerits, W. Deng and K. Han, *Angew. Chem., Int. Ed.*, 2018, **57**, 5359–5363.

96 L. Zhou, Y.-F. Xu, B.-X. Chen, D.-B. Kuang and C.-Y. Su, *Small*, 2018, **14**, 1703762.

97 J.-L. Xie, Z.-Q. Huang, B. Wang, W.-J. Chen, W.-X. Lu, X. Liu and J.-L. Song, *Nanoscale*, 2019, **11**, 6719–6726.

98 B. Yang, F. Hong, J. Chen, Y. Tang, L. Yang, Y. Sang, X. Xia, J. Guo, H. He, S. Yang, W. Deng and K. Han, *Angew. Chem., Int. Ed.*, 2019, **58**, 2278–2283.

99 J. T. Lee, S. Seifert and R. Sardar, *Chem. Mater.*, 2021, **33**, 5917–5925.

100 K. Kundu, P. Acharyya, K. Maji, R. Sasmal, S. S. Agasti and K. Biswas, *Angew. Chem., Int. Ed.*, 2020, **59**, 13093–13100.

101 L. Lian, G. Zhai, F. Cheng, Y. Xia, M. Zheng, J. Ke, M. Gao, H. Liu, D. Zhang, L. Li, J. Gao, J. Tang and J. Zhang, *CrystEngComm*, 2018, **20**, 7473–7478.

102 Z. Qi, X. Fu, T. Yang, D. Li, P. Fan, H. Li, F. Jiang, L. Li, Z. Luo, X. Zhuang and A. Pan, *Nano Res.*, 2019, **12**, 1894–1899.

103 S. P. Chaudhary, S. Bhattacharjee, V. Hazra, S. Shyamal, N. Pradhan and S. Bhattacharyya, *Nanoscale*, 2022, **14**, 4281–4291.

104 Y.-X. Feng, G.-X. Dong, K. Su, Z.-L. Liu, W. Zhang, M. Zhang and T.-B. Lu, *J. Energy Chem.*, 2022, **69**, 348–355.

105 J. Huang, S. Zou, J. Lin, Z. Liu and M. Qi, *Nano Res.*, 2021, **14**, 4079–4086.

106 Z. Liu, H. Yang, J. Wang, Y. Yuan, K. Hills-Kimball, T. Cai, P. Wang, A. Tang and O. Chen, *Nano Lett.*, 2021, **21**, 1620–1627.

107 Q. Li, T. Song, Y. Zhang, Q. Wang and Y. Yang, *ACS Appl. Mater. Interfaces*, 2021, **13**, 27323–27333.

108 Z. J. Bai, S. Tian, T. Q. Zeng, L. Chen, B. H. Wang, B. Hu, X. Wang, W. Zhou, J. B. Pan, S. Shen, J. K. Guo, T. L. Xie, Y. J. Li, C. T. Au and S. F. Yin, *ACS Catal.*, 2022, **12**, 15157–15167.

109 Q. M. Sun, J. J. Xu, F. F. Tao, W. Ye, C. Zhou, J. H. He and J. M. Lu, *Angew. Chem., Int. Ed.*, 2022, **61**, e202200872.

110 B. M. Bresolin, P. Sgarbossa, D. W. Bahnemann and M. Sillanpaa, *Sep. Purif. Technol.*, 2020, **251**, 117320.

111 G. Zhang, C. Yuan, X. Li, L. Yang, W. Yang, R. Fang, Y. Sun, J. Sheng and F. Dong, *Chem. Eng. J.*, 2022, **430**, 132974.

112 Z. Zhang, M. Wang, Z. Chi, W. Li, H. Yu, N. Yang and H. Yu, *Appl. Catal., B*, 2022, **313**, 121426.

113 Y. Yang, Z. Chen, H. Huang, Y. Liu, J. Zou, S. Shen, J. Yan, J. Zhang, Z. Zhuang, Z. Luo, C. Yang, Y. Yu and Z. Zou, *Appl. Catal., B*, 2023, **323**, 122146.

114 Z. P. Zhang, B. Z. Wang, H. B. Zhao, J. F. Liao, Z. C. Zhou, T. H. Liu, B. C. He, Q. Wei, S. Chen, H. Y. Chen, D. B. Kuang, Y. Li and G. C. Xing, *Appl. Catal., B*, 2022, **312**, 121358.

115 A. Mahmoud Idris, S. Zheng, L. Wu, S. Zhou, H. Lin, Z. Chen, L. Xu, J. Wang and Z. Li, *Chem. Eng. J.*, 2022, **446**, 137197.

116 L. Wu, S. Zheng, H. Lin, S. Zhou, A. Mahmoud Idris, J. Wang, S. Li and Z. Li, *J. Colloid Interface Sci.*, 2023, **629**, 233–242.

117 S. E. Creutz, E. N. Crites, M. C. De Siena and D. R. Gamelin, *Nano Lett.*, 2018, **18**, 1118–1123.

118 K. Chen, X. Deng, R. Goddard and H. Tüysüz, *Chem. Mater.*, 2016, **28**, 5530–5537.

119 N. Chen, T. Cai, W. Li, K. Hills-Kimball, H. Yang, M. Que, Y. Nagaoka, Z. Liu, D. Yang, A. Dong, C.-Y. Xu, R. Zia and O. Chen, *ACS Appl. Mater. Interfaces*, 2019, **11**, 16855–16863.

120 M. Liu, H. Ali-Loytty, A. Hiltunen, E. Sarlin, S. Qudsia, J.-H. Smatt, M. Valden and P. Vivo, *Small*, 2021, **17**, 2100101.

121 Z. Shi, Z. Cao, X. Sun, Y. Jia, D. Li, L. Cavallo and U. Schwingenschlögl, *Small*, 2019, **15**, 1900462.

122 Q. Han, X. Bai, Z. Man, H. He, L. Li, J. Hu, A. Alsaedi, T. Hayat, Z. Yu, W. Zhang, J. Wang, Y. Zhou and Z. Zou, *J. Am. Chem. Soc.*, 2019, **141**, 4209–4213.

123 Q. Liu, Y. Zhou, J. Kou, X. Chen, Z. Tian, J. Gao, S. Yan and Z. Zou, *J. Am. Chem. Soc.*, 2010, **132**, 14385–14387.

124 L.-Y. Wu, M.-R. Zhang, Y.-X. Feng, W. Zhang, M. Zhang and T.-B. Lu, *Sol. RRL*, 2021, **5**, 2100263.

125 R. Marschall, *Adv. Funct. Mater.*, 2014, **24**, 2421–2440.

126 J. Low, C. Jiang, B. Cheng, S. Wageh, A. A. Al-Ghamdi and J. Yu, *Small Methods*, 2017, **1**, 1700080.

127 M. Ma, H. Wang and H. Liu, *Chin. Chem. Lett.*, 2021, **32**, 3613–3618.

128 X. Liu, Q. Zhang and D. Ma, *Sol. RRL*, 2020, **5**, 2000397.

129 X. Lang, X. Chen and J. Zhao, *Chem. Soc. Rev.*, 2014, **43**, 473–486.

130 C. Yang, R. Li, K. A. I. Zhang, W. Lin, K. Landfester and X. Wang, *Nat. Commun.*, 2020, **11**, 1239.

131 T. Wang, D. Yue, X. Li and Y. Zhao, *Appl. Catal., B*, 2020, **268**, 118399.

132 D. Wu, X. Zhao, Y. Huang, J. Lai, J. Yang, C. Tian, P. He, Q. Huang and X. Tang, *J. Phys. Chem. C*, 2021, **125**, 18328–18333.

133 Y. Dai, C. Poidevin, C. Ochoa-Hernandez, A. A. Auer and H. Tüysüz, *Angew. Chem., Int. Ed.*, 2020, **59**, 5788–5796.

134 B.-M. Bresolin, S. B. Hammouda and M. Sillanpää, *J. Photochem. Photobiol., A*, 2019, **376**, 116–126.

135 Y. F. Zhu, Y. F. Liu, Q. Ai, G. H. Gao, L. Yuan, Q. Y. Fang, X. Y. Tian, X. Zhang, E. Egap, P. M. Ajayan and J. Lou, *ACS Mater. Lett.*, 2022, **4**, 464–471.

136 S. W. Zhao, S. H. Jin, H. M. Liu, Y. X. Su, W. Liu, S. F. Li, C. C. She, H. N. Li and K. Chen, *ChemCatChem*, 2022, **14**, e202101539.

137 S. Park, W. J. Chang, C. W. Lee, S. Park, H.-Y. Ahn and K. T. Nam, *Nat. Energy*, 2016, **2**, 16185.

138 H. Nishiyama, T. Yamada, M. Nakabayashi, Y. Maehara, M. Yamaguchi, Y. Kuromiya, Y. Nagatsuma, H. Tokudome, S. Akiyama, T. Watanabe, R. Narushima, S. Okunaka, N. Shibata, T. Takata, T. Hisatomi and K. Domen, *Nature*, 2021, **598**, 304–307.

139 H. Zhao, Y. Li, B. Zhang, T. Xu and C. Wang, *Nano Energy*, 2018, **50**, 665–674.

140 Y. Tang, C. H. Mak, C. Wang, Y. Fu, F. F. Li, G. Jia, C. W. Hsieh, H. H. Shen, J. C. Colmenares, H. Song, M. Yuan, Y. Chen and H. Y. Hsu, *Small Methods*, 2022, **6**, e2200326.

141 H. Zhao, K. Chordiya, P. Leukkunen, A. Popov, M. Upadhyay Kahaly, K. Kordas and S. Ojala, *Nano Res.*, 2020, **14**, 1116–1125.

142 L. Romani, A. Speltini, C. N. Dibenedetto, A. Listorti, F. Ambrosio, E. Mosconi, A. Simbula, M. Saba, A. Profumo, P. Quadrelli, F. De Angelis and L. Malavasi, *Adv. Funct. Mater.*, 2021, **31**, 2104428.

143 Y. Ji, M. She, X. Bai, E. Liu, W. Xue, Z. Zhang, K. Wan, P. Liu, S. Zhang and J. Li, *Adv. Funct. Mater.*, 2022, **32**, 2201721.

144 Y. Jiang, K. Li, X. Wu, M. Zhu, H. Zhang, K. Zhang, Y. Wang, K. P. Loh, Y. Shi and Q.-H. Xu, *ACS Appl. Mater. Interfaces*, 2021, **13**, 10037–10046.

145 G. Chen, P. Wang, Y. Wu, Q. Zhang, Q. Wu, Z. Wang, Z. Zheng, Y. Liu, Y. Dai and B. Huang, *Adv. Mater.*, 2020, **32**, e2001344.

146 C. Zhang, J. Chen, L. Kong, L. Wang, S. Wang, W. Chen, R. Mao, L. Turyanska, G. Jia and X. Yang, *Adv. Funct. Mater.*, 2021, **31**, 2100438.

147 S. M. S. U. Eskander and S. Fankhauser, *Nat. Clim. Change*, 2020, **10**, 750–756.

148 J. Pi, X. Jia, Z. Long, S. Yang, H. Wu, D. Zhou, Q. Wang, H. Zheng, Y. Yang, J. Zhang and J. Qiu, *Adv. Energy Mater.*, 2022, **12**, 2202074.

149 D. Wu, X. Zhao, Y. Huang, J. Lai, H. Li, J. Yang, C. Tian, P. He, Q. Huang and X. Tang, *Chem. Mater.*, 2021, **33**, 4971–4976.

150 Z. H. Cui, P. Wang, Y. Q. Wu, X. L. Liu, G. Q. Chen, P. Gao, Q. Q. Zhang, Z. Y. Wang, Z. K. Zheng, H. F. Cheng, Y. Y. Liu, Y. Dai and B. B. Huang, *Appl. Catal., B*, 2022, **310**, 121375.

151 S. Kumar, I. Hassan, M. Regue, S. Gonzalez-Carrero, E. Rattner, M. A. Isaacs and S. Eslava, *J. Mater. Chem. A*, 2021, **9**, 12179–12187.

152 J. Estrada-Pomares, S. Ramos-Terrón, G. Lasarte-Aragonés, R. Lucena, S. Cárdenas, D. Rodríguez-Padrón, R. Luque and G. de Miguel, *J. Mater. Chem. A*, 2022, **10**, 11298–11305.

153 Z. H. Cui, Y. Q. Wu, S. H. Zhang, H. Fu, G. Q. Chen, Z. Z. Lou, X. L. Liu, Q. Q. Zhang, Z. Y. Wang, Z. K. Zheng, H. F. Cheng, Y. Y. Liu, Y. Dai, B. B. Huang and P. Wang, *Chem. Eng. J.*, 2023, **451**, 138927.

154 B. M. Bresolin, N. O. Balayeva, L. I. Granone, R. Dillert, D. W. Bahnemann and M. Sillanpaa, *Sol. Energy Mater. Sol. Cells*, 2020, **204**, 110214.

155 M. Shi, H. Zhou, W. Tian, B. Yang, S. Yang, K. Han, R. Li and C. Li, *Cell Rep. Phys. Sci.*, 2021, **2**, 100656.

156 Q. Sun, W. Ye, J. Wei, L. Li, J. Wang, J.-H. He and J.-M. Lu, *J. Alloys Compd.*, 2022, **893**, 162326.

157 Z.-J. Bai, Y. Mao, B.-H. Wang, L. Chen, S. Tian, B. Hu, Y.-J. Li, C.-T. Au and S.-F. Yin, *Nano Res.*, 2022, DOI: 10.1007/s12274-022-4835-z.

158 Z. Wang, M. Liu, F. Xiao, G. Postole, H. Zhao and G. Zhao, *Chin. Chem. Lett.*, 2022, **33**, 653–662.

159 D. Wu, Y. Tao, Y. Huang, B. Huo, X. Zhao, J. Yang, X. Jiang, Q. Huang, F. Dong and X. Tang, *J. Catal.*, 2021, **397**, 27–35.

160 X. Wang, S. Yang, H. Li, W. Zhao, C. Sun and H. He, *RSC Adv.*, 2014, **4**, 42530–42537.

161 L. Cao, D. Ma, Z. Zhou, C. Xu, C. Cao, P. Zhao and Q. Huang, *Chem. Eng. J.*, 2019, **368**, 212–222.

162 B. Sarwan, A. D. Acharya, S. Kaur and B. Pare, *Eur. Polym. J.*, 2020, **134**, 109793.

163 C. Aydogan, G. Yilmaz, A. Shegiwal, D. M. Haddleton and Y. Yagci, *Angew. Chem., Int. Ed.*, 2022, **61**, e202117377.

164 C. Ye, J.-X. Li, Z.-J. Li, X.-B. Li, X.-B. Fan, L.-P. Zhang, B. Chen, C.-H. Tung and L.-Z. Wu, *ACS Catal.*, 2015, **5**, 6973–6979.